DEVELOPMENTAL NEUROSCIENCE

Mutations in *BCOR*, a co-repressor of *CRX/OTX2*, are associated with early-onset retinal degeneration

Maéva Langouët[1]†, Christine Jolicoeur[1]†, Awais Javed[1]‡, Pierre Mattar[1]§||, Micah D. Gearhart[2], Stephen P. Daiger[3], Mette Bertelsen[4,5], Lisbeth Tranebjærg[4,6], Nanna D. Rendtorff[4], Karen Grønskov[4], Catherine Jespersgaard[4]¶, Rui Chen[7], Zixi Sun[8], Hui Li[8], Najmeh Alirezaie[9], Jacek Majewski[9], Vivian J. Bardwell[2], Ruifang Sui[8]*, Robert K. Koenekoop[10]*, Michel Cayouette[1,11,12]*

Many transcription factors regulating the production, survival, and function of photoreceptor cells have been identified, but little is known about transcriptional co-regulators in retinal health and disease. Here, we show that BCL6 co-repressor (BCOR), a Polycomb repressive complex 1 factor mutated in various cancers, is involved in photoreceptor degenerative diseases. Using proteomics and transcription assays, we report that BCOR interacts with the transcription factors CRX and OTX2 and reduces their ability to activate the promoters of photoreceptor-specific genes. CUT&RUN sequencing further shows that BCOR shares genome-wide binding profiles with CRX/OTX2, consistent with a general co-repression activity. We also identify missense mutations in human *BCOR* in five families that have no evidence of cancer but present severe early-onset X-linked retinal degeneration. Last, we show that the human *BCOR* mutants cause degeneration when expressed in the mouse retina and have enhanced repressive activity on OTX2. These results uncover a role for BCOR in photoreceptors in both health and disease.

INTRODUCTION

Inherited retinal degenerations (IRDs) are characterized by photoreceptor cell death and account for the major part of worldwide blindness and low vision (*1*). Genome-wide association studies and next-generation sequencing have helped identify pathogenic variants in more than 250 genes causing IRDs (https://sph.uth.edu/retnet/). Together, these variants explain only around 60% of all cases, indicating that many disease-causing genes remain unknown. As the roles of photoreceptor-specific genes have been extensively explored in IRDs, it is likely that ubiquitously expressed genes with crucial functions in photoreceptors explain some of the unsettled cases.

In mammals, rod and cone photoreceptors are generated from a pool of multipotent retinal progenitor cells. Several transcription factors and nuclear receptors have been identified as essential players in photoreceptor cell specification, differentiation, and function (*2*, *3*). Among these, OTX2 and CRX, two related homeobox transcription factors, play essential roles in photoreceptor development and survival. In the mouse retina, OTX2 triggers *Crx* expression at around embryonic day 11.5 (E11.5) (*4*), and both factors then bind to a common DNA consensus sequence to control transcription (*5*–*7*). However, *Otx2*- and *Crx*-deficient retinas show different phenotypes, indicating distinct functions in retinal development (*7*, *8*). In *Otx2* conditional knockout (KO) retinas, photoreceptor cells are not generated (*4*, *9*), whereas photoreceptor production is unaltered in $Crx^{-/-}$ retinas, but expression of genes associated with phototransduction is reduced, eventually leading to photoreceptor degeneration (*10*). Later work has shown that CRX cooperates with the neural retina leucine (NRL) zipper transcription factor to promote expression of rod-specific genes (*11*–*14*). In humans, mutations in *CRX* have been associated with various IRDs (*15*), showing the critical role of this gene and its regulatory networks in photoreceptor survival. As CRX/OTX2 control the expression of *Rhodopsin* (*Rho*), which causes photoreceptor cell death when under- or overexpressed (*16*–*19*), understanding how CRX/OTX2 transcriptional activity is precisely regulated is crucial, but this remains unclear.

The activity of transcription factors is generally fine-tuned by transcriptional co-regulators, but very few have been studied in the retina. More specifically, the role of transcriptional co-repressors in photoreceptor biology is largely unexplored. Heterozygous null mutations in the X-linked BCL6 co-repressor (BCOR) (*20*), a ubiquitously expressed nuclear protein that also interacts with the Polycomb group proteins (PcG) (*21*), have been found in female patients with oculo-facio-cardio-dental (OFCD) syndrome [Online Mendelian Inheritance in Man (OMIM), #300166], a rare genetic condition that includes eye abnormalities such as microphthalmia and coloboma (*22*–*24*). Similarly, male *Bcor* KO mice die embryonically

[1]Cellular Neurobiology Research Unit, Institut de Recherches Cliniques de Montréal (IRCM), Montréal, QC H2W 1R7, Canada. [2]Department of Genetics, Cell Biology and Development, Development Biology Center, Masonic Cancer Center, University of Minnesota, Minneapolis, MN 55455, USA. [3]EHGED Department, Human Genetics Center, School of Public Health, University of Texas HSC, Houston, TX 77030, USA. [4]Department of Clinical Genetics, Rigshospitalet, The Kennedy Centre, Copenhagen, Denmark. [5]Department of Ophthalmology, Rigshospitalet, The Kennedy Centre, Glostrup, Denmark. [6]Institute of Clinical Medicine, University of Copenhagen, Denmark. [7]Department of Molecular and Human Genetics, Baylor College of Medicine, One Baylor Plaza, Houston, TX 77030, USA. [8]Department of Ophthalmology, State Key Laboratory of Complex Severe and Rare diseases, Peking Union Medical College Hospital, Chinese Academy of Medical Science and Peking Union Medical College, Beijing 100730, China. [9]Department of Human Genetics, McGill University, Montreal, QC, Canada. [10]Departments of Pediatric Surgery, Human Genetics, Adult Ophthalmology and the McGill Ocular Genetics Laboratory, McGill University Health Center Research Institute, Montreal, QC, Canada. [11]Department of Medicine, Université de Montréal, Montreal, QC, Canada. [12]Department of Anatomy and Cell Biology, Division of Experimental Medicine, McGill University, Montreal, QC, Canada.
*Corresponding author. Email: hrfsui@163.com (R.S.); robkoenekoop@hotmail.com (R.K.K.); michel.cayouette@ircm.qc.ca (M.C.)
†These authors contributed equally to this work.
‡Present address: Centre Medico Universitaire, University de Geneve, Geneva, Switzerland.
§Present address: Department of Cell and Molecular Medicine, University of Ottawa, Ottawa, ON K1H 8M5, Canada.
||Present address: Ottawa Health Research Institute (OHRI), Ottawa, ON K1H 8L6, Canada.
¶Present address: Danish National Genome Center, Copenhagen, Denmark.

with defects in optic cup formation (*25*, *26*), whereas heterozygous females develop OFCD-like defects (*26*), supporting a role for *Bcor* in eye development. However, because the eye does not develop normally in both human and mouse BCOR mutants, the later role of BCOR in the mature retina remains unknown.

In this study, we show that BCOR functions as a co-repressor for CRX/OTX2 in the mouse retina, modulating photoreceptor gene expression levels in a PcG-independent manner. We also identify new variants in human *BCOR* (*hBCOR*) that do not cause eye development defects or microphthalmia but are associated with early-onset photoreceptor degeneration in five different families.

RESULTS

Bcor is expressed in the developing and adult mouse and human retina

To explore a potential role for *Bcor* in the retina, we first determined its spatiotemporal expression in mice. In accordance with previously published RNA sequencing (RNA-seq) datasets (fig. S1, A and B) (*27*, *28*) and in situ hybridization analysis (*29*), we found expression of *Bcor* transcripts from as early as E13.5 in the retinal progenitor cell layer and ganglion cell layer. *Bcor* expression was stable during retinal development and persisted in all cell layers in the adult retina (fig. S1C). Consistently, mouse BCOR (mBCOR) protein was expressed in all cell layers from embryonic to adult stages (Fig. 1, A and B). As predicted (*21*, *26*), we found mBCOR in the nucleus, with a typical "ring" pattern staining in adult rod photoreceptors, which have an inverted nuclear chromatin organization (*30*, *31*), and classical nuclear pattern in cones interspersed between chromocenters (Fig. 1A), suggesting that mBCOR is associated with euchromatin rather than heterochromatin. We also characterized the expression of *hBCOR* transcripts by analyzing previously published single-cell RNA-seq (scRNA-seq) datasets (*32*). We found that hBCOR is expressed in all cell types in the human retina, including rod and cone photoreceptors (Fig. 1C), as observed in mice. These data are consistent with a potential role for BCOR in retinal development, maintenance, and/or function.

BCOR negatively regulates expression of photoreceptor-specific genes

To gain molecular insights into BCOR function in the mammalian retina, we performed whole transcriptome sequencing on mouse retinal cells after down-regulation of *Bcor*. We used a previously validated short hairpin RNA (shRNA) designed against mouse *Bcor* (*shBcor*) (*33*) and confirmed its efficiency in reducing BCOR protein levels in the retina (Fig. 2, A and B). We then electroporated P0 retinas in vivo with expression vectors coding for a scramble shRNA and *GFP* (*sh-scramble-GFP* or Ctrl) or *shBcor* and *GFP*, sorted green fluorescent protein–positive (GFP^+) cells at postnatal day 21 (P21), and carried out RNA-seq. Among the differentially expressed transcripts, we found classical rod photoreceptor genes in the up-regulated group, such as *Rho*, *Gnat1*, *Cnga1*, *Abca4*, *and Rp1* (Fig. 2C and table S1A). Consistently, BCOR knockdown in retinal progenitor cells at P0 in vivo led to a significant up-regulation of *Rho* transcript levels by quantitative reverse transcription polymerase chain reaction (qRT-PCR) (Fig. 2D). Gene ontology (GO) term analysis revealed enrichment of genes associated with photoreceptor biology in this up-regulated group of transcripts (Fig. 2E and table S1, B and C). Conversely, the GO terms analysis of the down-regulated group of transcripts contained genes associated with synapses, neuronal projections,

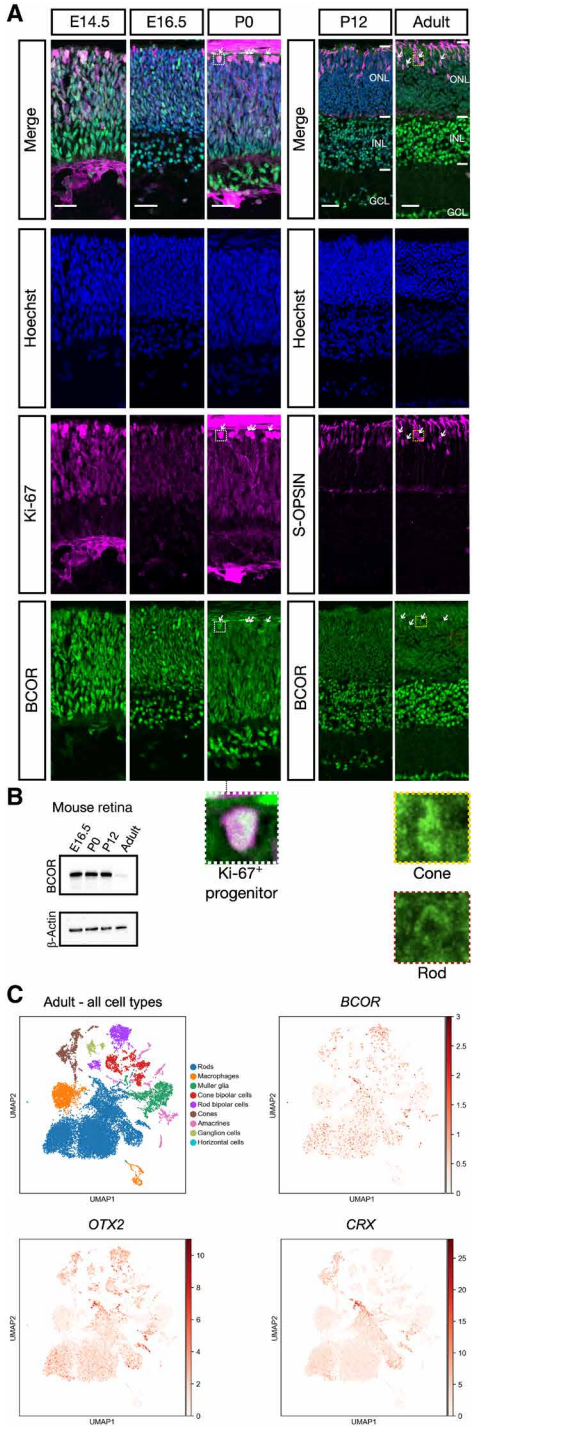

Fig. 1. BCOR is expressed in the mouse and human retina. (**A**) BCOR immunostaining in the mouse retina at different stages, as indicated. Progenitor cells were costained with Ki-67 and S-cones with S-OPSIN. Boxed regions show high magnification of BCOR staining in one $Ki\text{-}67^+$ progenitor from the P0 panel (white), one cone (yellow), and one rod (red). White arrows indicate $BCOR^+/S\text{-}OPSIN^+$ cones in the adult condition and $Ki\text{-}67^+$ progenitors in the P0 condition. Scale bars, 30 μm. INL, inner nuclear layer; ONL, outer nuclear layer; GCL, ganglion cell layer. (**B**) Immunoblot for BCOR from total retinal extracts at different stages. (**C**) Uniform Manifold Approximation and Projection (UMAP) plots showing *BCOR*-, *OTX2*-, and *CRX*-expressing cells among clustered cell types detected in previously published human adult postmortem retina scRNA-seq datasets (*32*).

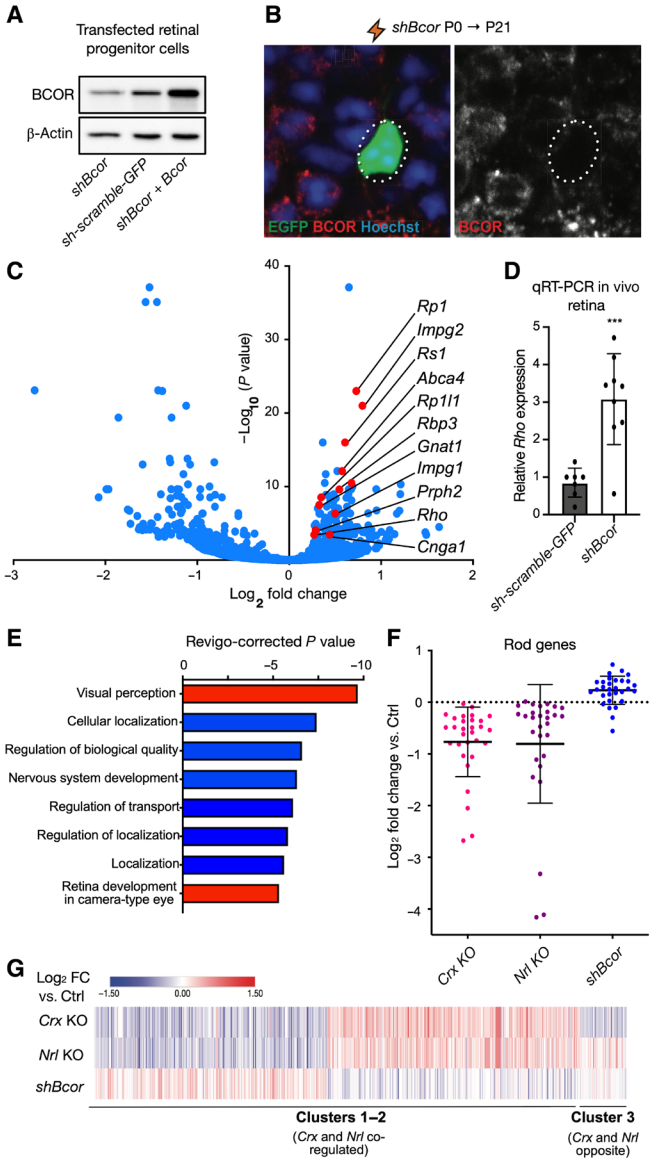

Fig. 2. BCOR regulates expression of photoreceptor-specific genes. (**A**) Immunoblot for BCOR and β-actin from retinal cell culture extracts, 4 days after transfection of E17 retinal progenitors with *sh-scramble-GFP* expression vector (Ctrl), *shBcor*, or *shBcor* coexpressed with a version of *Bcor* lacking the 3′ untranslated region (UTR) region targeted by the shRNA. (**B**) High-magnification single *Z*-plane image of the photoreceptor layer stained for BCOR 21 days after in vivo electroporation of *Bcor* shRNA (*shBcor*) and *sh-scramble-GFP* expression vectors at P0. GFP$^+$ electroplated cell lacking BCOR signal is highlighted by a dotted circle. (**C**) Volcano plot of control-transfected ($n = 2$) and *shBcor*-transfected ($n = 2$) retinas. GFP$^+$ cells were sorted from P21 retinas and profiled by RNA-seq. Red data points represent rod-specific genes. (**D**) qRT-PCR analysis of *Rho* mRNA expression from sorted GFP$^+$ cells 7 days after electroporation of either *sh-scramble-GFP* alone (ctrl, $n = 7$) or *shBcor* + GFP (*shBcor*, $n = 9$) at P0 in vivo. Data are plotted as means ± SD; ***$P < 0.001$, unpaired two-tailed *t* test. (**E**) Revigo-corrected GO analysis on genes differentially regulated by *shBcor*, as determined by DeSeq2 (Benjamini-Hochberg adjusted $P < 0.05$) (*73*, *74*). (**F**) Scatter plot of rod-specific gene expression changes in P21 *Crx* and *Nrl* KO retinas (*34*) versus *shBcor* [30 rod-specific genes as defined in (*35*)]. (**G**) Heatmap analysis of the same datasets shown in (F) but widened to all genes differentially regulated by CRX and NRL. Note that gene expression changes in cluster 3 are opposite for *Crx* and *Nrl* (possibly cone transcripts), whereas the changes are similar between *Crx* and *Nrl* in clusters 1 and 2, indicating that these are rod-specific transcripts.

and neuron development (table S1D), like *Kif5a*, *CalB2*, *Nefm*, *Kif5c*, *Kcnc1*, and *Chd3*. Together, these results are consistent with a possible role for BCOR in retinal neuron cell development and function.

Next, we compared our data to previously published RNA-seq datasets of *Crx*$^{-/-}$ and *Nrl*$^{-/-}$ mouse models (GSE52006) (*34*), also performed at P21. When focusing on rod-specific genes, as defined in (*35*), we found that genes down-regulated in *Crx* and *Nrl* KOs are generally up-regulated after BCOR knockdown (Fig. 2F). When we merged all differentially expressed genes identified in the *Crx*$^{-/-}$ and *Nrl*$^{-/-}$ datasets [fold change cutoff at 2, FPKM (fragments per kilobase of transcript per million mapped read) value > 2, and adjusted $P < 0.05$] with our *shBcor* dataset, we found that gene clusters 1 and 2, which correspond to rod-specific transcripts down-regulated in both *Crx*$^{-/-}$ and *Nrl*$^{-/-}$ retinas, have the opposite up-regulation in the *shBcor* condition (Fig. 2G and table S2). Cluster 3, which contains cone-specific transcripts, is down-regulated in *Crx*$^{-/-}$ retinas but up-regulated in both *Nrl*$^{-/-}$ and *shBcor* conditions. Together, these results suggest that BCOR is a negative regulator of photoreceptor gene expression.

BCOR function does not depend on interaction with the Polycomb complex in the retina

As BCOR is a component of a noncanonical PcG repressive complex 1 (ncPRC1.1) (*21*, *36*, *37*), we suspected that it might regulate photoreceptor gene expression through its ability to bind PcG proteins. To test this hypothesis, we used a conditional *Bcor* floxed (*Bcor*^{Fl}) mouse allele (*26*), which contains loxP sites before exon 9 and after exon 10, allowing CRE-dependent production of a truncated BCOR protein (BCORΔE9-10) lacking the PCGF1 interaction domain (PUFD), which was reported to render BCOR unable to associate with the ncPRC1.1 complex (*36*, *38*). We crossed *Bcor*$^{Fl/+}$ females to α*Pax6-Cre*; *Bcor*$^{Fl/Y}$ males (see Materials and Methods for details), in which *Cre* is expressed in progenitors of the peripheral retina from E10 onward (*39*), to generate a BCOR$^{\Delta E9\text{-}10}$ mouse line, which includes female *Bcor*$^{\Delta E9\text{-}10/\Delta E9\text{-}10}$ and male *Bcor*$^{\Delta E9\text{-}10/Y}$ mice (referred to as *Bcor*$^{\Delta E9\text{-}10}$ mice from now on, unless otherwise specified). As predicted, exons 9 and 10 were deleted in the peripheral retina of *Bcor*$^{\Delta E9\text{-}10}$ mice (fig. S2A), resulting in the expression of a truncated BCORΔE9-10 protein (fig. S2B) that is unable to interact with PCGF1 (*36*, *38*), although we cannot exclude indirect interaction with PCGF1 through adaptor proteins that would interact with other parts of BCOR. Using a panel of retinal cell type–specific markers (see Materials and Methods), we examined the global morphology and number of marker-positive cells in peripheral retinas in adult animals aged 45 to 300 days. Unexpectedly, we did not detect any major changes in cell numbers compared to control littermates (fig. S2, C and D) and photoreceptor gene expression was unchanged (fig. S2E). Although we cannot totally exclude that *Bcor*$^{\Delta E9\text{-}10}$ mice might have more subtle phenotypes undetected here, these results suggest that, unlike several other tissues, the function of BCOR in the retina does not depend on interaction with PcG protein, at least for cell type production and photoreceptor gene regulation, suggesting a mechanism involving unknown partners.

BCOR interacts with CRX and OTX2

To identify novel partners of BCOR in the retina, we used tandem affinity purifications followed by mass spectrometry (IP-MS) from P10 mouse retinal extracts. As predicted, we identified members of the ncPRC1.1 complex including KDM2B, PCGF1, RING2, SKP1,

RING1, and CBX8, validating the approach, but also many non-PRC partners such as proteins associated with transcription and splicing, as well as multiple histones (table S3). One of the hits corresponded to CRX/OTX2. Because CRX and OTX2 have high amino acid homology, it was difficult to determine which of these two proteins was pulled down with BCOR. Four of seven peptides were specific to CRX, two were common to both CRX and OTX2, and one was specific to OTX2.

To determine whether BCOR interacts with both CRX and OTX2, or more specifically with only one of the proteins, we cotransfected constructs expressing *Bcor* together with *Crx* or *Otx2* in human embryonic kidney (HEK) 293T cells, immunoprecipitated BCOR, and blotted for CRX or OTX2. We found that BCOR interacts with both CRX and OTX2 (Fig. 3A), validating our IP-MS data. BCOR also coimmunoprecipitated with CRX and OTX2 from P7 to P9 retinal extracts, indicating interaction in vivo (Fig. 3B). Using a proximity ligation assay (PLA) on adult retinal sections, we further showed that BCOR is in close physical proximity to CRX/OTX2 in photoreceptors and bipolar cells, which also express OTX2 and CRX (*8*, *40*), whereas no signal was detected with a control cytoplasmic protein (PKCα) also expressed in bipolar cells (Fig. 3C). On the basis of these data, we conclude that BCOR interacts with both CRX and OTX2 in the retina.

Given the lack of an obvious phenotype in the adult $Bcor^{\Delta E9\text{-}10}$ mice, we postulated that the truncated BCORΔE9-10 protein might still be able to interact with CRX/OTX2. Consistently, coimmunoprecipitation (coIP) in HEK 293T cells showed a clear interaction of BCORΔE9-10 with both CRX and OTX2 (fig. S2F). In parallel, we conducted PLA on adult $Bcor^{\Delta E9\text{-}10}$ retinas using the anti-BCOR antibody and found a clear proximity signal with CRX/OTX2 (fig. S2G). Last, using a construct driving expression of luciferase from the proopiomelanocortin (POMC) minimal promoter [−35/+63 base pairs (bp)] containing three CRX/OTX2 binding motifs (*41*), we showed activation of this promoter by OTX2 and significant repression of OTX2 activity when cotransfecting BCORΔE9-10 (fig. S2H). Overall, these results suggest that the truncated BCORΔE9-10 protein can still interact with CRX/OTX2 and is still able to repress OTX2 function, potentially explaining the absence of detectable phenotype in the mouse mutant retina.

BCOR is generally present at genomic regions bound by CRX/OTX2

We next assessed the genomic distribution of BCOR in the retina by CUT&RUN (C&R) sequencing at E14, P0, and adult stages (*42*). As BCOR interacts with CRX and OTX2, we predicted that it might occupy similar genomic regions. To test this prediction, we compared the BCOR C&R profile to that of CRX/OTX2 (the antibody used recognizes both CRX and OTX2) and to a published adult CRX-specific chromatin immunoprecipitation sequencing (ChIP-seq) dataset (*5*) (tables S4 and S5). Using Hypergeometric Optimization of Motif EnRichment (HOMER), we assessed the binding motifs present in the CRX/OTX2 C&R sequencing and found that, among the top target peaks, the expected canonical "TAATCC" or variant "TAATCG" motifs (*6*, *7*) have the highest *P* value (fig. S3A).

We next examined the genome-wide distribution of BCOR-, CRX/OTX2-, and CRX-specific peaks. At E14, we found that CRX/OTX2 and BCOR have more promoter-bound peaks compared to intronic and distal intergenic regions (Fig. 4A). At P0 and adult stage, however, CRX/OTX2 and CRX-only peaks are displaced

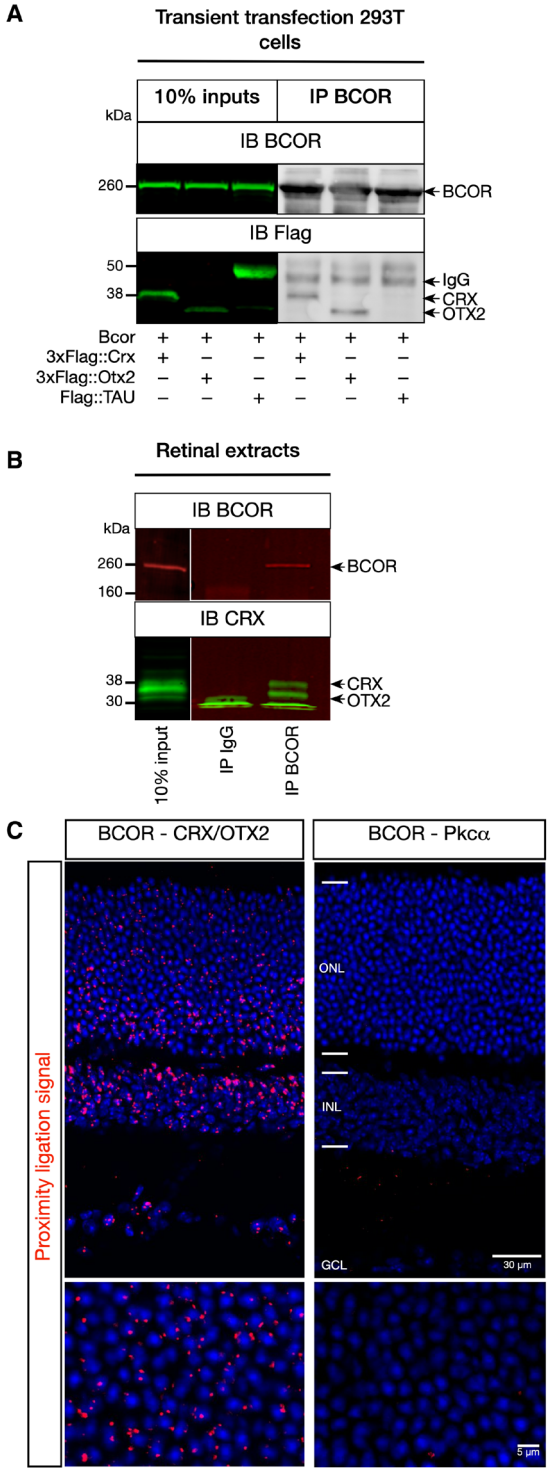

Fig. 3. BCOR interacts with CRX and OTX2. (**A**) BCOR coimmunoprecipitates with CRX and OTX2 when coexpressed in HEK 293T cells. The microtubule-binding protein TAU was used as a negative control. (**B**) BCOR (red) coimmunoprecipitates with CRX and OTX2 (green) from P7 to P9 total retinal protein extracts. (**C**) Proximity ligation assay (PLA; red signal) on adult mouse retinal sections for BCOR and CRX/OTX2. PLA for BCOR and the cytoplasmic protein PKCα was used as a negative control. Blue represents Hoechst. Scale bars, 30 μm (top panel) and 5 μm (bottom zoom-in panel).

away from the promoters to the intronic or intergenic regions, whereas the peaks for BCOR remain mostly at promoters.

By conducting a GO term annotation analysis, we found that BCOR peaks at E14 and P0 are associated with genes corresponding to the PcG complexes and other DNA-associated complexes regulating transcription, splicing, and chromatin modifications (fig. S3B), and some of these associated GO terms were shared with CRX/OTX2. In adult, photoreceptor biology GO terms were strongly associated with BCOR peaks (fig. S3B). To further validate the specificity of BCOR peaks, we ran several quality control analyses comparing our BCOR data with a variety of other genomic datasets. First, when aligned to previously published NRL ChIP-seq dataset (*43*), another key photoreceptor transcription factor, our BCOR C&R dataset exhibited little overlap with NRL peaks (fig. S3C). Second, we compared the E14 C&R BCOR dataset with previously published ATAC-seq (assay for transposase-accessible chromatin using sequencing) and ChIP-seq datasets of several chromatin marks in the retina (H3K4me1, H3K4me2, H3K4me3, H3K27ac, and H3K27me3) (*44*). BCOR exhibited little overlap with chromatin marks enriched at enhancers or bivalent/repressed regions (fig. S3D). BCOR occupancy also overlapped with only a small percentage of the overall accessible regions determined via ATAC-seq (fig. S3,

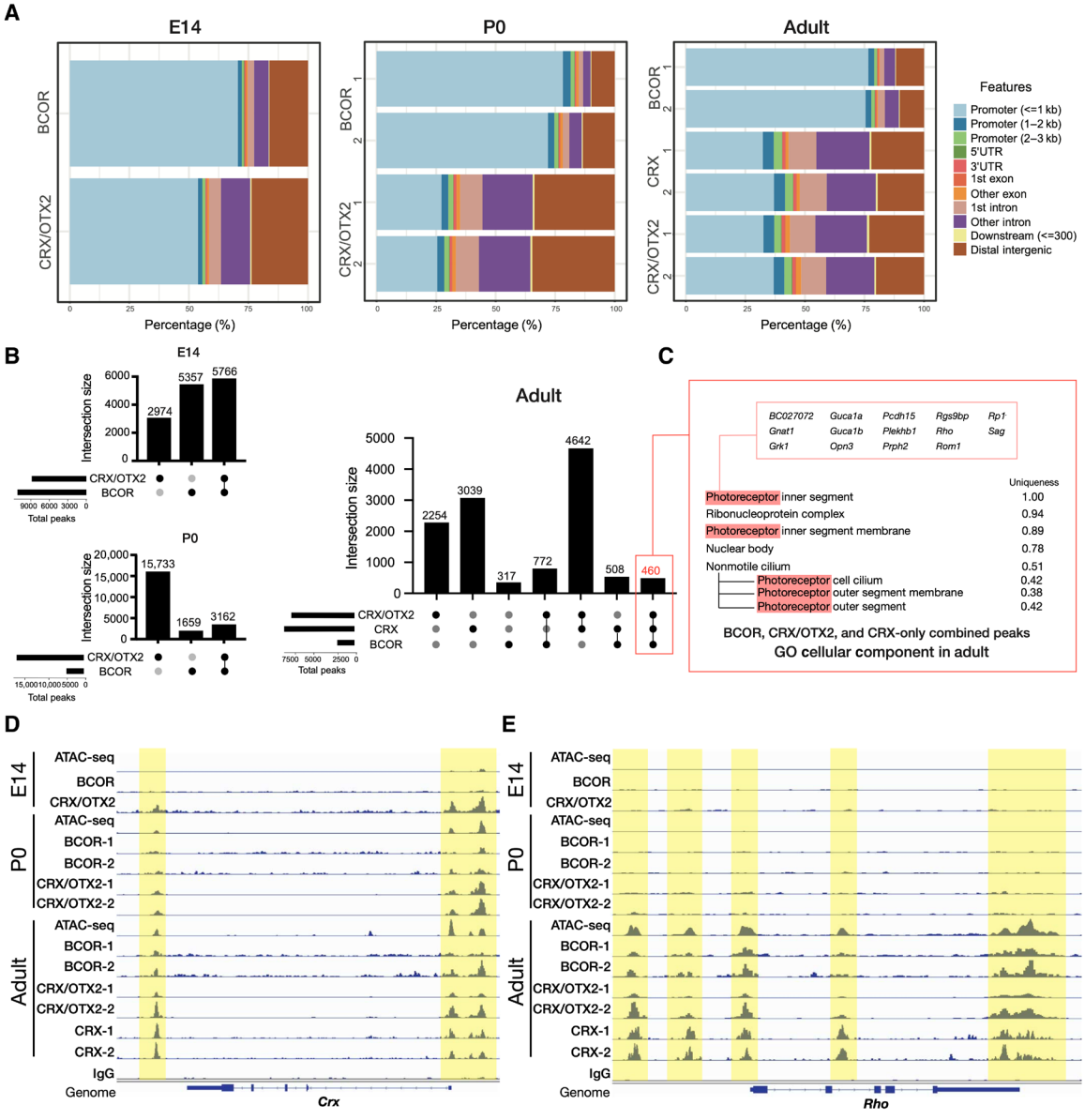

Fig. 4. BCOR and CRX/OTX2 bind common genomic targets. (**A**) Histograms representing preferentially bound regions in the genome for each replicate of BCOR and CRX/OTX2 C&R and published CRX-only ChIP-seq (*5*). (**B**) UpSet plots representing the combinatorial binding overlap between pooled replicates of BCOR and CRX/OTX2 C&R at E14 and P0, as well as CRX-only ChIP-seq in adult. The lower left scale indicates the total number of peaks per sample. (**C**) Revigo-corrected GO analysis results for combinatorial peaks in adult. Genes associated with the "photoreceptor" GO category are the most unique terms. (**D** and **E**) Chromatin landscapes from E14, P0, and adult retinas across a 15-kb segment of the mouse genome for BCOR, CRX/OTX2, and immunoglobulin G (IgG) control C&R, CRX-only ChIP-seq, and published ATAC-seq (*44*) over the *Crx* (D) and (E) *Rho* genes. Tracks are autoscaled by stages allowing direct comparison. Regions of interest are highlighted in yellow.

D and E). Last, photoreceptor genes were enriched in regions co-occupied by BCOR and CRX/OTX2, in agreement with our shRNA experimental results (Fig. 2C and fig. S3E).

Next, we characterized the genome-wide overlap in DNA binding between BCOR, CRX/OTX2, and CRX-specific peaks. We observed overlap in genomic binding at each stage (Fig. 4B and table S6), and BCOR and CRX/OTX2 combinatorial binding at the *Crx* promoter as early as P0 (Fig. 4D), supporting a developmental role for BCOR. While intersection analysis shows a large reduction in co-occupied regions in adults, GO annotation analysis of shared peaks in adults demonstrated that these 460 peaks were mostly in genes involved in photoreceptor biology, such as photoreceptor inner segment, photoreceptor cell cilium, and photoreceptor outer segment (Fig. 4, B and C, and fig. S3B). When we looked more closely at the genes in the GO lists, we found key rod photoreceptor genes such as *Rho*, *Rom1*, *Sag*, *Gnat1*, and *Grk1* (Fig. 4C and table S6). Detailed examination of the photoreceptor gene loci showed enrichment of BCOR, CRX/OTX2, and CRX at the *Rho* promoter (Fig. 4E). This enrichment was specific to adult stages, as we did not observe occupancy to *Rho* at E14 or P0, suggesting a role for BCOR in the regulation of adult photoreceptor gene expression, rather than broad chromatin silencing, as previously reported in stem cells and early embryonic development (*36*, *45*, *46*).

Last, we intersected the adult BCOR C&R dataset with the *shBcor* RNA-seq dataset and previously published histone mark ChIP-seq (*44*). When focusing on differentially expressed genes identified in the *Bcor* knockdown RNA-seq, we found BCOR peaks near the transcription start site for two-thirds of those genes (fig. S3E). Cluster 2 showed that the presence of both CRX/OTX2 and BCOR and GO term analysis revealed again enrichment for genes with photoreceptor-related function (tables S7 and S8). However, cluster 3 genes are all associated with H3K27me3 and are not bound by BCOR. We suggest that, instead, those genes are probably bound by the PcG complex version depleted of BCOR (PRC1/2) and might be misregulated through the well-defined PcG biology.

These results show that BCOR is generally found at the same genomic regions as CRX/OTX2 during retinal development. Together with our finding that BCOR interacts with CRX/OTX2, these results suggest that BCOR may be a co-regulator of CRX/OTX2 activity.

BCOR is a co-repressor for CRX and OTX2

As reducing BCOR protein levels increases *Rho* expression (Fig. 2, C and D) and BCOR binds to the *Rho* promoter (Fig. 4E), we hypothesized that BCOR might negatively regulate *Rho* promoter activity. To test this idea, we transfected P0 retinal explants with a *pRHO*-luciferase reporter construct, together with *shBcor*, and tested the activity of the promoter 5 days later. We observed that *shBcor* leads to a significant up-regulation of *RHO* promoter activity, which was abolished when coexpressing *shBcor* with a version of *Bcor* lacking the 3′ untranslated region (UTR) region targeted by the shRNA (Fig. 5A). Because we previously observed the opposite changes on rod-specific gene expression following *shBcor* treatment compared to $Nrl^{-/-}$ (Fig. 2F), we postulated that BCOR might also affect the mouse *Nrl* promoter activity. As predicted, we found that *shBcor* increases *Nrl* promoter activity, whereas this effect is rescued by an exogenous source of *Bcor* insensitive to the shRNA (Fig. 5B).

Because the *RHO* promoter is bound by CRX, OTX2, and NRL, we could not discriminate whether BCOR influences *RHO* promoter activity through its interaction with CRX and OTX2 or via modulation of *Nrl* in these experiments. To distinguish between these possible mechanisms, we used a promoter assay in HEK 293T cells, a heterologous system in which retina-specific genes are not expressed. We found that CRX or OTX2 transfection in these cells increased *pRHO*-luciferase activity, as predicted, and that BCOR coexpression significantly represses this effect (Fig. 5C). These results indicate that BCOR can repress CRX/OTX2 activity independently of NRL. To ask whether the repression activity of BCOR may require binding at regions of the *RHO* promoter that are not bound by CRX/OTX2, we transfected rat fibroblasts with a construct driving expression of luciferase from the POMC minimal promoter (−35/+63 bp) containing three CRX/OTX2 binding motifs (*41*). As predicted, we observed activation of this promoter with OTX2, but this was significantly repressed by cotransfecting BCOR (Fig. 5D). As the POMC minimal promoter is unrelated to the *RHO* promoter and contains only CRX/OTX2 binding motifs, these results suggest that BCOR repression activity on CRX/OTX2 is direct and argue against a mechanism involving modulation via NRL. Thus, the effect of BCOR on the Nrl promoter observed in Fig. 5B is likely a consequence of the co-repression activity of BCOR on CRX/OTX2.

Our alignment of BCOR C&R data to NRL ChIP-seq dataset showed no significant overlap between NRL and BCOR peaks (fig. S3C), and NRL did not show up in our BCOR IP-MS (table S3), suggesting that the two proteins are unlikely to interact. To provide further evidence of this, we performed in vivo IP and NanoBiT assays with BCOR and NRL and failed to detect any evidence of interaction (fig. S4, A and B). While we cannot exclude that action of BCOR on the *Nrl* promoter might additionally play a role in vivo, these results strongly suggest that BCOR is a direct co-repressor for CRX/OTX2 proteins.

Because fine regulation of *Rho* expression levels is critical to photoreceptor survival, we predicted that reducing BCOR expression might lead to reduced photoreceptor cell numbers. Consistently, we found that electroporation of *shBcor* in P0 mouse retinas in vivo leads to a small but significant reduction in photoreceptor cell numbers at P21 (Fig. 5, E and F).

BCOR variants are associated with early-onset retinitis pigmentosa

The above results point to a critical role for mBCOR in photoreceptor cell biology, but whether this is also the case in humans was unknown. To determine whether hBCOR variants might be involved in IRD, we screened patients for which known IRD mutations had been excluded and that presented with a clinical evaluation of early-onset progressive photoreceptor degeneration from retinitis pigmentosa (RP) or cone-rod dystrophy. The patients recruited showed loss of retinal architecture, severe retinal thinning, loss of autofluorescence, and some presented total loss of both rod and cone-mediated electroretinogram (ERG) signals, without any other major clinical manifestations (Fig. 6A, Table 1, and fig. S5).

To identify the disease-causing gene, we performed whole-exome sequencing (WES) on two affected siblings from family I (I.3 and I.4) and their mother (I.2), who is mildly affected (Fig. 6B). We found a hemizygous variant in *BCOR* (NM_017745.5) in the two affected siblings: c.3461A>G leading to p.Glu1154Gly, where the negatively charged glutamic acid is replaced by a smaller neutral glycine (Fig. 6C). This variant was heterozygous in the mother, and validation sequencing confirmed cosegregation in the family (Fig. 6B). Moreover, this change was not found in genome aggregation database

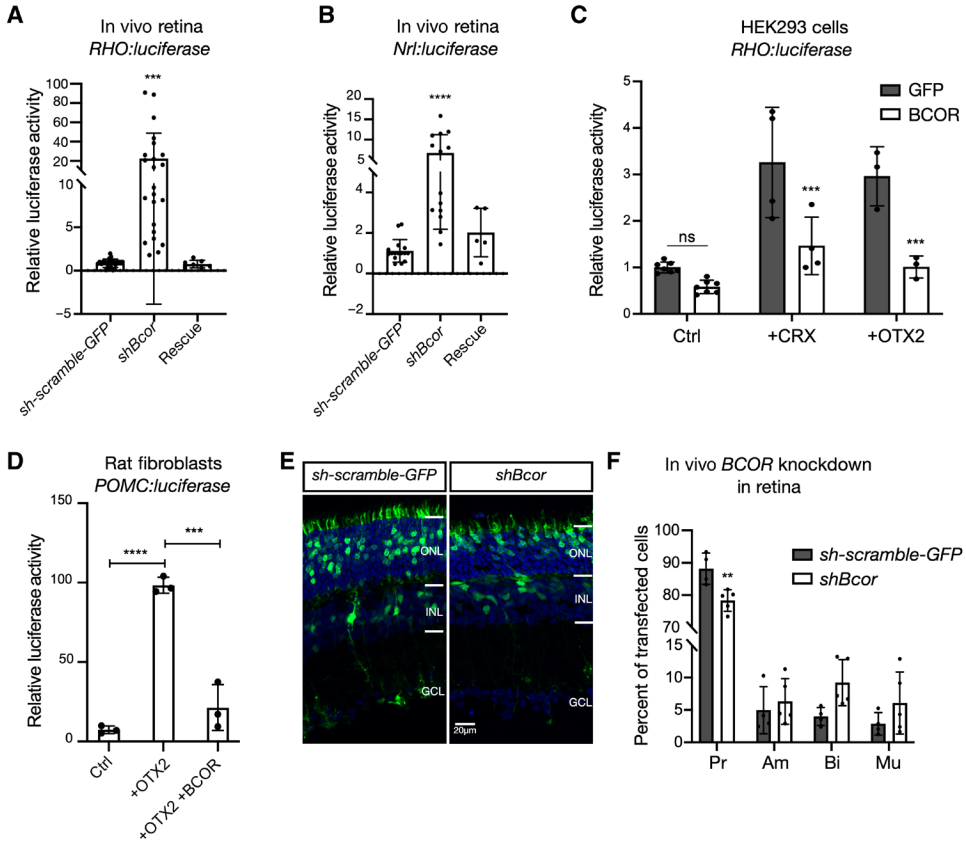

Fig. 5. BCOR regulates *Rho* and *Nrl* promoter activity and influences cell fate decisions. (**A** and **B**) Luciferase assays on retinal lysates from explants collected 5 days (A) or 2 days (B) after electroporation at P0 with an *sh-scramble-GFP* vector (Ctrl), *shBcor*, or *shBcor* with a version of *Bcor* lacking the 3′UTR region targeted by the shRNA (rescue), together with *pRHO*-luciferase (A) or *pNrl*-luciferase (B). Data are shown as relative activity of the reporter over the *sh-scramble-GFP* control condition. (A) Ctrl, $n = 24$; *shBcor*, $n = 23$; Rescue, $n = 7$ and (B) Ctrl, $n = 16$; *shBcor*, $n = 14$; Rescue, $n = 5$. Data are plotted as means ± SD; $^{***}P < 0.001$, $^{****}P < 0.0001$, one-way analysis of variance (ANOVA) test with Dunnett's posttest. (**C**) Luciferase assay on cell lysates from HEK 293T cells 24 hours after transfection with a *pRHO*-luciferase reporter together with *GFP* or *BCOR* alone (Ctrl, $n = 7$) or with *Crx* (+CRX, $n = 4$) or *Otx2* (+OTX2, $n = 3$). Data are shown as means ± SD and represent relative activity of the reporter over the GFP control condition. $^{***}P < 0.001$, two-way ANOVA test with Bonferroni posttest. ns, not significant. (**D**) Luciferase assay on cell lysates from rat fibroblasts 24 hours after transfection with a $(GE3)_3$-*POMC*-luciferase reporter together with *GFP*, *OTX2*, or *OTX2* + *BCOR* ($n = 3$). Data are shown as means ± SD and represent relative activity of the reporter over the GFP control condition. $^{***}P < 0.001$, $^{****}P < 0.0001$, one-way ANOVA test with Tukey's test correction. (**E**) Examples of electroporated areas in P21 retinal sections following electroporation of *sh-scramble-GFP* or *shBcor* at P0 in vivo. (**F**) Quantification of the proportion of different cell types over total transfected cells 21 days following *GFP* ($n = 4$) or *shBcor* ($n = 5$) electroporation at P0 in vivo. Pr, photoreceptors; Bi, bipolar cells; Am, amacrine cells; Mu, Müller cells. Data are plotted as means ± SD; $^{**}P < 0.01$, $^{***}P < 0.001$, two-way ANOVA with a Sidak test correction.

(gnomAD), Exome Variant Server (EVS), The 1000 Genome Browser (1KGP), or our internal control databases and was predicted deleterious by four different types of in silico analyses: CADD (Combined Annotation Dependent Depletion) (*47*), SIFT (Sorting Intolerant From Tolerant) (*48*), PolyPhen-2 (Polymorphism Phenotyping) (*49*), and MutationTaster (*50*) (Table 1). Because WES did not reveal any other changes in known or candidate retinal genes that cosegregated with the disease in this family, we considered *BCOR* a prime candidate to explain the clinical manifestations.

To determine whether mutations in the same gene might be shared in other patients for which IRD remained genetically unexplained, we used the European Retinal Degeneration Consortium (ERDC) database, which contains WES and WGS (whole-genome sequencing) results from IRD patients who are unsettled for known IRD genes. We identified four additional *BCOR* mutations from four other families, which were confirmed by Sanger sequencing. Cosegregation in the families was validated and revealed variable penetrance in heterozygous females, ranging from unaffected to severe. These variants were predicted to be deleterious by in silico analyses: CADD scores >15, SIFT close to 0, PolyPhen-2 and MutationTaster close to 1 (Table 1). The missense mutations included c.2055G>C, c.1901C>A, c.1448C>T, and c.553A>G, leading to p.Leu685Phe, p.Pro634Gln, p.Pro483Leu, and p.Ser185Gly, respectively (Fig. 6, A to C, and Table 1). The *BCOR* variants were highly conserved on the basis of GERP (Genomic Evolutionary Rate Profiling), PhyloP-100, and nucleotide alignments (Fig. 6D) and essentially absent from normal control databases such as ExAC (Exome Aggregation Consortium) and EVS. The four additional variants were all clustered around the BCL6 binding site of BCOR, but not directly within it (Fig. 6E). These five families did not harbor variants in any known IRD genes.

Together, these findings indicate that the *BCOR* mutations identified in five different families cause a severe, diffuse, and degenerative photoreceptor disease. None of the patients or their family

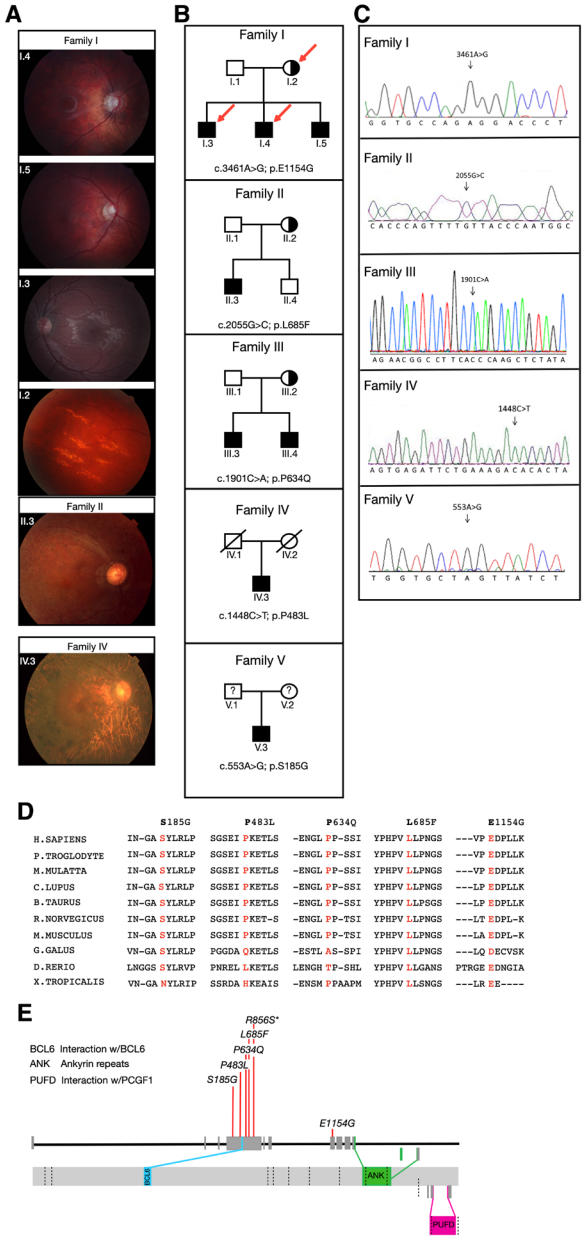

Fig. 6. Missense mutations in *BCOR* underlie a previously-unknown form of early-onset RP. (**A**) Fundus photographs of patients from families I, II, and IV: I.4 and I.5, depicting significant titled disc configuration with peripapillary atrophy and mild vascular attenuation; I.3, demonstrating unremarkable appearance of the retina and the heterozygous mother; I.2, showing atypical sectoral linear retinal hypopigmentation; II.3, showing mottled retinal hypopigmentation and severely attenuated vasculature; and IV.3, showing diffuse retinal atrophy with perimacular bone spicule pigmentation and vascular attenuation. (**B**) Pedigrees of five families with X-linked RP affecting males (squares, filled symbols) and associated missense mutations. Heterozygous females (circles) show variable expressivity with symptoms ranging from unaffected to severe (half-filled symbols). Red arrows in family I indicate individuals analyzed by WES (I.2, I.3, and I.4). (**C**) Sanger sequence analysis representing each familial mutation identified. (**D**) *BCOR* sequence conservation across 10 species of each mutated amino acid identified. (**E**) Simplified map representing the *BCOR* gene. Coding exons are denoted by gray boxes, and introns are denoted by the black horizontal line. Colored boxes represent exons associated with respective protein domain, as indicated. The position of the *BCOR* mutations identified is indicated across the map with a red vertical bar.

members had OFCD syndrome or other *BCOR*-related diseases, like cancer or colobomas.

Expression of hBCOR mutants in the mouse retina leads to degeneration

The identification of five *BCOR* mutations in patients from five different families presenting with retinal degeneration strongly suggested that these mutants cause the pathology. However, to provide more direct evidence, we electroporated constructs encoding the *P483L*, *L685F*, and *E1154G* human mutant *BCOR* (*mutBCOR*) identified in patient families in the mouse retina at P0 and analyzed retinal histology 60 days later. In addition, we expressed an engineered artificial mutation (c.2568A>T leading to R856S) in the 3′ region of the exon containing the BCL6 interaction domain. Given that four of the five mutations identified in humans were located in this exon, we wanted to test whether variants in this region would generally affect BCOR function. To avoid potential confounding effects of the endogenous BCOR, we simultaneously knocked down *mBcor* using an shRNA that does not target *hBCOR*. We first verified the levels of expression obtained 7 days after electroporation by qRT-PCR on GFP$^+$ sorted cells and found about a fivefold increase in *BCOR* transcript levels (fig. S6A). We also confirmed that expression of BCOR does not alter cell fate decisions by counting cell type proportions 2 weeks after electroporation, when retinal development is complete (fig. S6B). While we observed only minor morphological changes in the *shBcor*-only and *shBcor* + *wtBCOR* conditions, retinas expressing *mutBCOR* had severe photoreceptor degeneration (Fig. 7, A and B), which was accompanied by important reactive gliosis, as shown by swelling and complexification of Müller glia morphology (Fig. 7C and fig. S6C), and increased glial fibrillary acidic protein (GFAP) expression compared to controls (Fig. 7D). Degeneration was so important for some *mutBCOR* that quantification of *BCOR* mutants separately was not always possible due to the low number of GFP$^+$ cells remaining at P60. Therefore, we designed a semiquantitative analysis of the "degeneration index" for each *mutBCOR*, which took into consideration the histological integrity of the retina, the thickness of the outer nuclear layer (ONL), the complexification and size of Müller glia, and the extent of GFAP expression in the electroporated regions (Fig. 7E). We found that all *mutBCOR* had a higher degeneration index on average than GFP or *wtBCOR* controls (Fig. 7F). The BCOR mutant E1154G, which is the only mutant identified that is located more downstream of the gene (close to the Ankyrin repeats), appeared to have a weaker effect. These results indicate that expression of human *mutBCOR* in the mouse retina leads to degeneration, supporting our conclusion that they cause disease in humans. Our finding that the engineered R856S BCOR mutant also produces similar effects suggests that the general area around the BCL6 binding domain is important for BCOR function.

To understand how the hBCOR mutations identified in patients might lead to photoreceptor cell death, we performed several experiments using either transient expression or stable cell lines expressing three of the newly discovered mutations in hBCOR: P483L, L685F, and E1154G, as well as the engineered R856S variant. First, we evaluated the degradation rate by blocking protein synthesis with cycloheximide and assessing protein decay kinetics via flow cytometry or Western blot but found that the hBCOR mutations do not affect protein stability (fig. S7A and not shown). Next, using coIP and BioID proteomics in cell lines, we found that the hBCOR mutants

Table 1. Clinical features of patients and in silico analysis of *BCOR* mutations. gnomAD: A collection of research articles and related content from the genome aggregation database (gnomAD) consortium that describes and analyzes human genetic variation. EVS: The Exome Variant Server was created as part of the NHLBI Exome Sequencing Project (ESP) and contains variant frequency information spanning normal humans of 6503 exomes. CADD: Combined Annotation Dependent Depletion is a tool for scoring the deleteriousness of single-nucleotide variants. Scores >15 are severely deleterious. SIFT: Sorting Intolerant From Tolerant amino acid substitutions predict whether an amino acid substitution in a protein will have a phenotypic effect. SIFT scores range from 0.0 (deleterious) to 1.0 (tolerated). PolyPhen-2: Polymorphism Phenotyping is a tool that predicts the impact of an amino acid substitution on the structure and function of a human protein using straightforward physical and comparative considerations. The PolyPhen-2 numerical score ranges from 0.0 (benign) to 1.0 (damaging). MutationTaster: A substitution tool. A value close to 1 indicates a high security of the prediction that the change is deleterious. GERP: Genomic Evolutionary Rate Profiling score (evolutionary conservation) > 4 is significant. PhyloP-100: PhyloP scores measure evolutionary conservation at individual alignment sites compared to the evolution that is expected under neutral drift. Positive PhyloP scores measure conservation, which is slower evolution than expected, at sites that are predicted to be conserved. Scores >2.7 are severe and deleterious. VA, visual acuity.

Family ($N = 6$)	I		II		III		IV	V
Pedigree number (coding)	MOGL3072		SRF701		RFS034		SRF779	BCM-1
Patients	3	4	5	3	2 (ID 03)	3 (ID 09)	4 (ID 10)	3	3
BCOR mutation (cDNA change)	c.3461A>G		c.2055G>C		c.1901C>A		c.1448C>T	c.533A>G
BCOR mutation (protein change)	p.E1154G		p.L685F		p.P634Q		p.P483L	p.S185G
gnomAD	0.0000		0.0000		0.00000000		0.000302	0.0000
EVS	0.0000		0.0000		0.0000		0.0000	0.0000
CADD	25.0000		24.0000		24.2000		23.1000	24.0000
SIFT	0.0900		0.0000		0.0100		0.5400	0.0100
PolyPhen-2	0.9950		0.9980		0.9440		0.9990	0.6050
MutationTaster	0.9996		0.9989		0.9994		0.9977	0.9997
GERP	5.4800		3.8400		5.7700		5.7700	5.5600
PhyloP-100	2.6840		2.0430		5.5680		1.5700	4.4800
Country of origin (culture)	Canada		China		United States		China	China
Sex	M	M	M	M	F	M	M	M	M
Final clinical diagnosis (XLRP or XLCRD)	XLCRD	XLCRD	XLCRD	XLRP	XLRP	XLRP	XLRP	XLRP	NA
Age at first evaluation (years)	15	13	12	20	14	12	12	30	NA
First symptom (central VA or color loss, peripheral loss, night blindness)	VA loss	VA loss	VA loss	Night blindness	Night blindness	Night blindness	Night blindness	Night blindness	NA
Retinal architecture loss (Y or N) age of onset if possible	N	N	N	Y	NA	NA	NA	Y	NA
Retinal thinning (Y or N) age of onset if possible	N	N	N	43	NA	NA	NA	NA	NA
Loss of autofluorescence (Y or N) age of onset when available	N	N	N	43	NA	NA	NA	NA	NA
Loss of ERG signals	NA	NA	NA	Y	NA	Y (rod and cone)	Y (rod and cone)	Y	NA
Score visual test	20/60	20/50	20/50	NA	NA	NA	NA	NA	NA
Age at legal or complete blindness (years)	No	No	No	45	62 (legal blindness)	61 (legal blindness)	62 (legal blindness)	50	NA
Presence of other symptoms	No	No	No	No	No	No	No	No	No

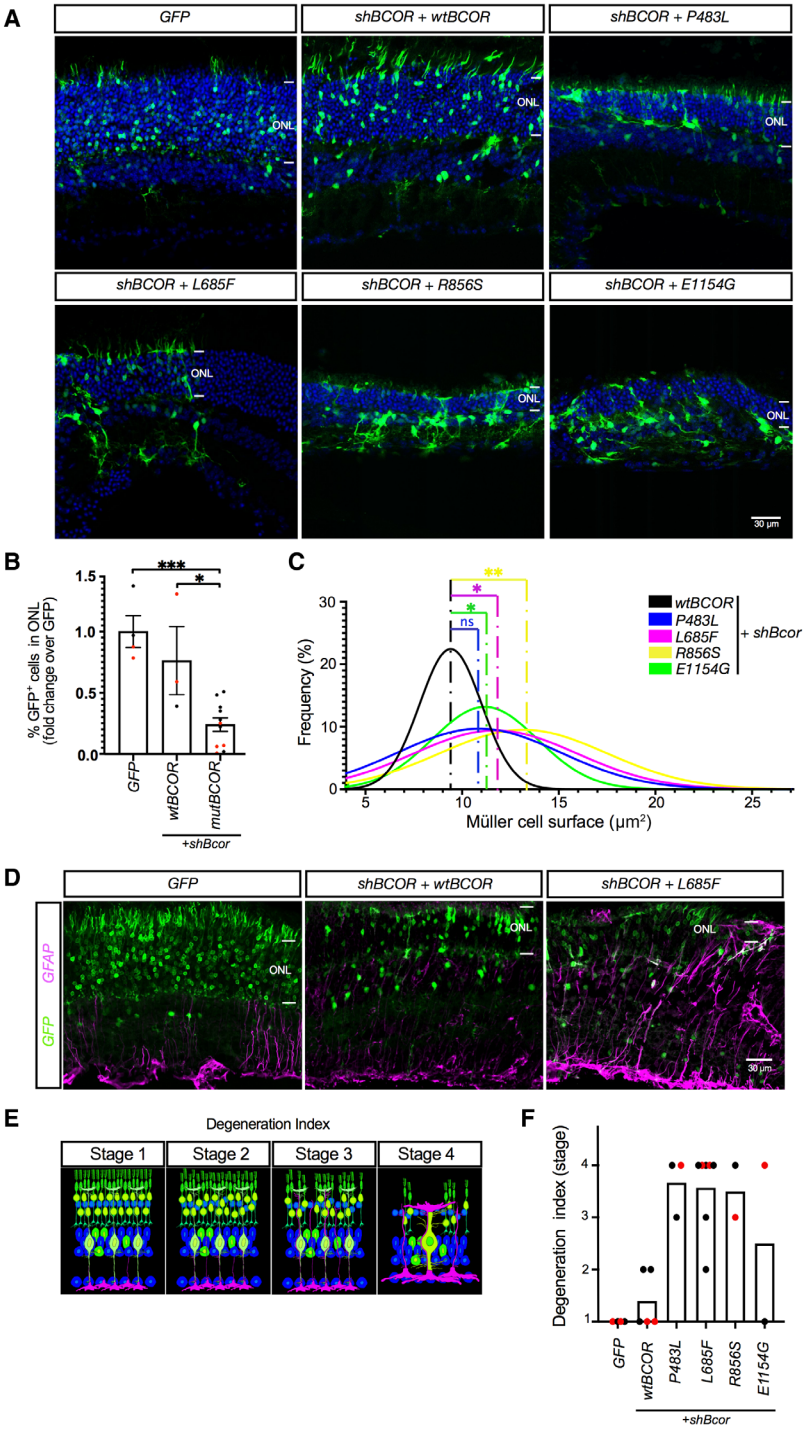

Fig. 7. Expression of human *BCOR* mutants in the mouse retina induce photoreceptor degeneration. (**A**) Examples of electroporated areas in retinal sections 60 days after electroporation of *GFP* alone, *shBcor-GFP* + *wtBCOR*, or *mutBCOR* (P483L, L685F, R856S*, E1154G) at P0 in vivo. Scale bar, 30 µm. (**B**) Percentage of GFP$^+$ cells in the photoreceptor layer (ONL) after expression of GFP alone (normalized to 1), *shBcor-GFP* + *wtBCOR*, or *mutBCOR*. Red data points, males; black data points, females. Bar graphs illustrate means ± SEM; *$P < 0.05$, ***$P < 0.01$, one-way ANOVA. (**C**) Distribution of Müller glia cell body surface (µm^2) 60 days after electroporation of *wtBCOR* or the different *mutBCOR* identified in the legend. Gaussian curve fit of Müller cell size distributions obtained from 36 cells for wtBCOR, 89 cells for P483L, 77 cells for L685F, 36 cells for R856S*, and 89 cells for E1154G. (**D**) Confocal images of electroporated regions (green) stained for GFAP (purple) 60 days after electroporation of *GFP* alone, *shBcor-GFP* + *wtBCOR*, or *mutBCOR* (L685F). Scale bar, 30 µm. (**E**) Illustration representing the semiquantitative analysis of degeneration index. Stage 1, normal changes observed after electroporation (rare rosettes and injection site visible); stage 2, slightly disorganized retina and layering with increased rosette frequency; stage 3, multiple area with rosettes, disorganized layers, and thinner photoreceptor layer; stage 4, severe degeneration with rosettes, disorganized layers, and low to no photoreceptors. (**F**) Average degeneration index following electroporation with *GFP* alone or *shBCOR* + *wtBCOR* or the different *mutBCOR*. Red data points, males; black data points, females. Total number of electroporated retinas analyzed (5 to 20 sections analyzed per retina): GFP = 4; wtBCOR = 5; P483L = 3; L685F = 7; R856S = 2; E1154G = 2.

are still able to interact with BCL6, MLLT3, PcG members, and OTX2 (fig. S7, B to E, and table S9). Last, to test whether the *BCOR* mutations might affect repression activity, we cotransfected HEK 293 cells with an OTX2 expression construct together with a reporter expressing luciferase from the POMC minimal promoter containing OTX2 binding sites (as done in Fig. 5D and fig. S2H) and the BCOR mutants. As predicted, we observed a strong activation of the promoter when cotransfecting OTX2, which was repressed by *wtBCOR* (Fig. 8, A and B). The concentration required to obtain 50% repression of OTX2 [half-maximal inhibitory concentration (IC_{50})] was significantly lower, however, with three of the four *mutBCOR* tested (Fig. 8B), indicating that their repression activity is enhanced compared to wtBCOR. As observed following expression in the mouse retina in vivo, mutant E1154G produced a milder phenotype compared to the other mutants tested. Protein expression levels were similar in all conditions (fig. S8A), excluding the possibility that differences in transfection efficiency might explain altered repression activity with *mutBCOR*. Cotransfection of a BCOR deletion mutant construct in which the region surrounding the BCL6 domain was removed (amino acids 408 to 513) lost the ability to repress OTX2 activity (fig. S8B), strongly suggesting that this deletion includes the interaction region with OTX2 or that it contains a critical co-repressor module. These results suggest that the BCOR mutations identified here have altered repression activity on OTX2, which disrupts the regulation of photoreceptor gene expression and eventually cause cell death.

DISCUSSION

In this study, we identify BCOR as a new interacting partner of the retinal transcription factors CRX and OTX2. We further show that BCOR functions as a co-repressor for CRX/OTX2 and generally binds the same genomic regions, thereby contributing to fine-tune photoreceptor gene expression levels. We uncover mutations in *BCOR* that cause early-onset IRDs in humans, pointing to a critical conserved role for BCOR in photoreceptor health and disease.

A key finding reported in this study is that BCOR interacts with CRX and OTX2 and functions as a co-repressor for these master retinal transcription factors. A BioGrid entry has recently reported a possible interaction between OTX2 and BCOR in a high-throughput

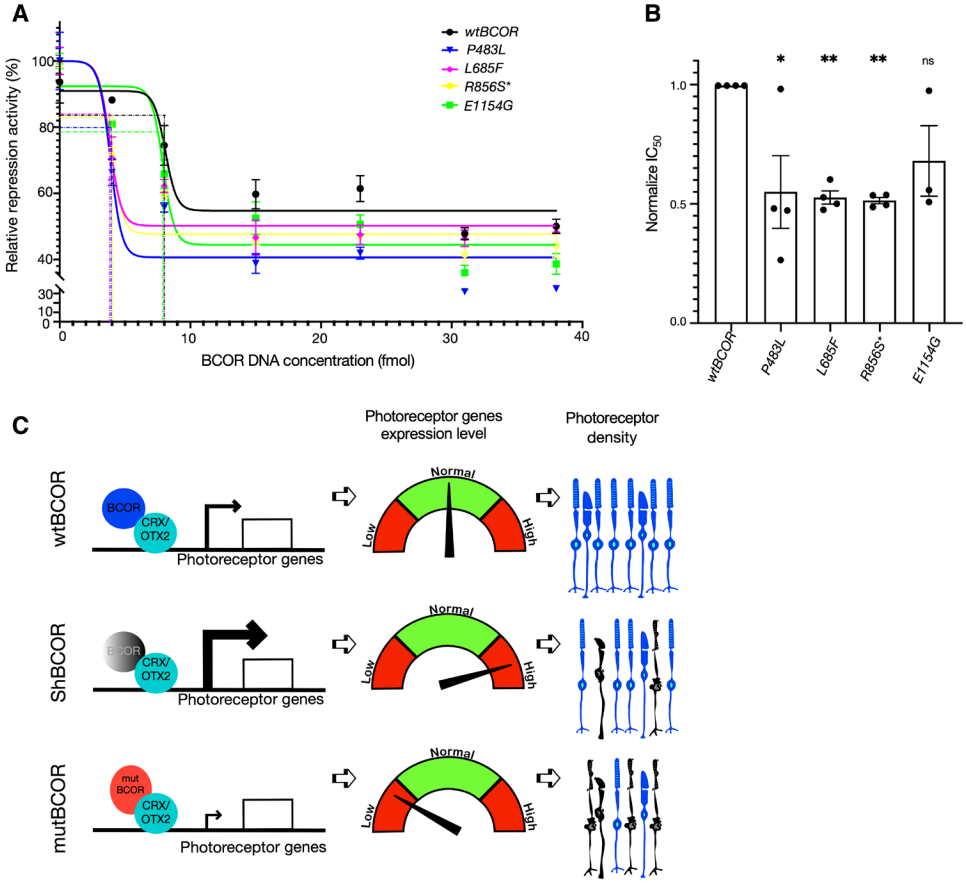

Fig. 8. Human BCOR mutants display enhanced repression activity on OTX2. (**A**) Representative dose-response curve of BCOR repression on OTX2 activity. (**B**) Normalized IC_{50} of BCOR DNA required to repress OTX2 activity. Graphs represent means ± SEM. *$P < 0.05$, **$P < 0.01$, one-way ANOVA. (**C**) Model of *BCOR* function in the retina: In normal retinas, BCOR fine-tunes expression of photoreceptor genes by acting as a co-repressor for CRX/OTX2, leading to normal levels of photoreceptor gene expression (top). When BCOR activity is reduced after expression of shBCOR (middle), CRX/OTX2-mediated activation of photoreceptor gene expression is increased, leading to abnormally high levels of expression and some photoreceptor degeneration. Upon BCOR mutant (mutBCOR) expression (bottom), co-repression on OTX2 is higher, which is predicted to reduce photoreceptor gene expression levels, leading to degeneration. Open boxes represent photoreceptor genes. Arrows indicate the transcription start site, and thickness is relative to level of transcriptional activity. CRX/OTX2, represented by light blue circles, is bound to photoreceptor gene promoters. Blue and black photoreceptors represent healthy and dying photoreceptors, respectively.

screen (https://thebiogrid.org/111055/summary/homo-sapiens/otx2.html), further supporting our results. We propose that the co-repressive activity of BCOR on CRX/OTX2 proteins is critical to precisely fine-tune photoreceptor gene expression levels, thereby ensuring long-term photoreceptor survival (Fig. 8C). As OTX2 levels are low in mature photoreceptors, however, we propose that the effect of BCOR is more likely through its interaction with CRX in these cells. Numerous studies in *Drosophila* and rodents demonstrated that altered *Rho* expression levels, for example, impairs photoreceptor cell function and survival (*16*–*19*, *51*–*54*). In addition, many mutations in the *RHO* gene have been identified in RP patients. Several of them lead to increased expression levels or activity, which become toxic to photoreceptors (*55*), highlighting the importance of precise modulation of *RHO* expression levels. As CRX and OTX2 are known to regulate the expression of many other photoreceptor genes, the co-repression activity of BCOR might have widespread effect. Our C&R data showing co-occupancy of BCOR at many critical CRX/OTX2 sites throughout the genome, in addition to RNA-seq results showing that multiple photoreceptor genes are deregulated after BCOR knockdown, support this interpretation. The relative stoichiometry of BCOR and CRX/OTX2 proteins at various genomic regions is likely to influence the precise levels of gene expression, but this remains to be explored. As we find that BCOR represses *Nrl* promoter activity, even though we failed to detect physical interaction between the two proteins, it is also possible that the effects we observe after BCOR manipulations lead to changes in *Nrl* activity, thereby contributing to BCOR function in photoreceptors.

Although not significant, we noted a tendency for increased bipolar and Müller glia cell number following *Bcor* knockdown (Fig. 5F). We therefore sorted the differentially expressed genes from our *shBcor* RNA-seq data into the retinal cell type–specific profiles defined using previously published Drop-seq analysis of single retinal cells (*56*). We found no major changes in the expression of genes specific to bipolar cells or Müller glia (fig. S9). These data suggest that BCOR acts on rod photoreceptor number and gene expression specifically, without affecting other cell types. It is important to note, however, that *Bcor* knockdown at P0 does not target early-born cell types, raising the possibility that BCOR may additionally function in these cells during development. It will be interesting to explore this possibility.

Our work suggests that the function of BCOR does not depend on interaction with the ncPRC1.1 complex, supporting a noncanonical role for BCOR in the retina. Given the strong phenotypes associated with inactivation of members of the PcG complexes (PRC1 or PRC2) in the mouse retina (*57*–*59*), the absence of retinal defect in $Bcor^{\Delta E9\text{-}10}$ animals was unexpected. Our data show that the truncated BCORΔE9-10 protein produced in the mutant mice can still interact with CRX and OTX2 and is still able to repress OTX2 activity, strongly suggesting that, unlike many other tissues where it has been studied, the truncated BCOR protein remains functional in the retina. Alternatively, BCORL1, the homolog of BCOR, which also carries the PUFD domain (*60*), might be compensating for the *Bcor* exon 9 and 10 deletion, although its expression level is low in the retina (*28*, *44*). It will be interesting to generate double KOs of *Bcor* and *Bcorl1* to explore this possibility.

Our study identifies the first *BCOR* mutations associated with IRD in humans, and our findings that expression of these mutants in the mouse retina leads to degeneration support the conclusion that they are causative. In addition, our data show that the BCOR mutants display enhanced repressive activity on OTX2 transactivation, providing a possible molecular explanation for the retinal degenerative disease observed in human patients harboring these mutations. An engineered BCOR mutant (R856S) located in the same exon as four of the five BCOR mutations identified in patient families produced similar effects in the in vivo expression studies and promoter assays, suggesting that the region surrounding the BCL6 interaction domain is important to BCOR function in the retina. On the basis of these results, we propose that enhanced BCOR repression on OTX2 results in reduced photoreceptor gene expression levels, which eventually leads to cell death (Fig. 8C). *BCOR* is well known for its role in cancer (*61*) and developmental syndromes (*23*, *26*). In the patients presented here, however, there is no evidence of such diseases, suggesting that the *BCOR* mutations we identified produce retina-specific phenotypes. Our finding that BCOR mutants still interact with classical partners like BCL6 and PcG components is consistent with the idea that the mutations do not affect canonical BCOR functions in other tissues. This could explain the absence of symptoms other than retinal degeneration in these patients.

With the development of adeno-associated viral vector (AAV)-based gene therapy for IRDs, receiving a genetic diagnosis becomes increasingly important. The identification of BCOR function in photoreceptor biology reported in this study opens avenues of research that may lead to the development of novel pharmacological and/or gene therapy approaches. Last, this work also points to the importance of transcriptional cofactors in IRDs, which have been largely neglected, broadening perspectives to identify other genes involved in monogenic Mendelian IRDs.

MATERIALS AND METHODS

Animal care

All animal work was performed in accordance with guidelines from the Institut de Recherches Cliniques de Montréal animal care committee and the Canadian Council on Animal Care. CD1 mice were obtained from Taconic. $Bcor^{Fl}$ (*26*) and α-*Pax6::Cre* (α-*Cre*) (*39*) alleles and genotyping protocols were previously described. Mice were also genotyped to exclude the presence of *rd8* alleles (*62*). See table S10 for primer sequences. The exact cross used to obtain litters analyzed in fig. S2 is α-*Pax6::Cre*+; $Bcor^{Fl/Y}$ *males to* $Bcor^{Fl/+}$ females.

Vectors

The pYX-ASC1-*Bcor* cDNA vector was obtained from Dharmacon (clone ID: 6412868) and corresponds to isoform c. The expression vector pCIG2, previously described, was modified to contain a Gateway destination cassette.

The pCAGGS-*BCOR*::Flag vector was obtained from P. Vanderhaeghen (*33*) and corresponds to isoform a (EFplink-FLAG-HA-BCORa-HIS). Point mutations in the *BCOR* open reading frame to obtain pCAGGS-*BCOR-L685F*::Flag, pCAGGS-*BCOR-P483L*::Flag, pCAGGS-*BCOR-R856S*::Flag, and pCAGGS-*BCOR-E1154G*::Flag were generated using a QuikChange lightning site-directed mutagenesis kit (Agilent) following the manufacturer's recommendations.

The pGL3b-human *RHODOPSIN* promoter (positions −181 to +49) luciferase (*pRHO*-luciferase) and the pCDNA3.1-3xFlag::*Crx* constructs were obtained from T. Furukawa. The *pNrl*-luciferase was modified from the plasmid p*Nrl*-DsRed obtained from Addgene (#13764) by replacing DsRed with firefly luciferase using the In-Fusion technology.

Renilla luciferase reporter vector pIS2-Renilla was obtained from Addgene (#12177). The p5XBCL6-SV40-luciferase reporter vector was previously described (*20*). The pßactin:LacZ was obtained from J. Cross.

The pCIG2-3xFlag::*Otx2* plasmid was generated using the In-Fusion technology to add a 3xFlag tag to the existing pCIG2-*Otx2* expression vector (splice variant 3) obtained from C. Schuurmans. RNA interference (RNAi) constructs *shBCOR* (targeting the 3′UTR of *BCOR*), *shBcor* (targeting the 3′UTR of *Bcor*), and scramble *shRNA* are expressed downstream of the U6 promoter into pSilencer2.1-CAG-Venus (pSCV2) vector and were obtained from P. Vanderhaeghen (*33*).

The expression vector pCIG2-Myc::*BCL6* was obtained from P. Vanderhaeghen (*33*). The entry clone containing the short POZ binding domain of *BCL6*, pDONOR221-*POZ-BCL6*, was generated by Gateway BP reaction (Thermo Fisher Scientific) from the pCIG2-Myc::*BCL6* vector (*20*). To generate the expression vector pGEX-4T-1-*POZ-BCL6*, the entry clone pDONOR221-*POZ-BCL6* was recombined using L/R Clonase II (Thermo Fisher Scientific) into pGEX-4T-1-Gateway.

The POG44 Flp-Recombinase expression vector, the pDest pCDNA5-FRT/TO-EGFP-N-term, and pCDNA5-FRT/TO-BirA-3xFlag-C-Term inducible expression vectors were obtained from A.-C. Gingras. All pCDNA5-FRT/TO expression clones were generated by recombination of the appropriate entry clone and pDest vector using L/R Clonase II (Thermo Fisher Scientific).

The $(CE3)_3$-POMC-luciferase vector was obtained from J. Drouin (*41*). The expression vectors pBit 1.1-TK-SmBit::*Nrl*, pBit 1.1-TK-SmBit::*Numb*, and pCAGGS-LgBit::*BCOR*::Flag for the NanoBiT assay were generated by In-Fusion cloning.

See table S10 for shRNA and primer sequences. See table S11 for a summary of all the vectors used in this study.

In vivo subretinal electroporation

In vivo subretinal electroporation of P0 eyes was performed as described previously (*63*) using plasmid DNA at 1 to 3 μg/μl. pSCV2-*shBcor* or scramble *shRNA* vector pSCV2 was used for loss-of-function experiments, and a mixture of pCIG2, pSCV2-*shBcor*, pSCV2-*shBcor* and pCAGGS-*BCOR*::Flag, pCAGGS-*BCOR-L685F*::Flag, pCAGGS-*BCOR-P483L*::Flag, pCAGGS-*BCOR-R856S*::Flag, or pCAGGS-*BCOR-E1154G*::Flag was used for gain-of-function experiments. The electroporated eyes were collected at P21 and P60, respectively, fixed, and processed for immunohistochemistry as described below.

Amaxa electroporation and retinal progenitor culture

E17 retinas from one litter of C57/B6J mouse line were collected, and cells were dissociated and cultured as previously described (*64*). In short, 0.75 million to 1.2 million of retinal progenitor cells were transfected with 10 μg of pSCV2, pSCV2-*shBcor*, or a combination of pSCV2-*shBcor* + pCIG2-*Bcor* using the Amaxa Rat Neural Stem Cell Nucleofector Kit (Lonza Walkersville Inc., #VPG-1004). Electroporation was carried out using program A-33 of the Amaxa Nucleofactor 2b device (Lonza Walkersville Inc., #AAB-1001). A total of 500,000 cells per well were plated on poly-L-lysine/laminin–coated six-well plates and grown for 4 days before harvest for Western blot analysis.

In situ hybridization

Plasmid pYX-ASC1-*Bcor* was used as a template for synthesizing the digoxigenin (Dig)–labeled RNA probes. The plasmid was linearized with Bam HI to prepare the template DNA for the probe synthesis. T3 RNA polymerase was used to synthesize the antisense probe, and T7 RNA polymerase was used to synthesize the sense control probe.

Eyes at developmental and adult stages were collected, fixed in 4% paraformaldehyde overnight at 4°C, washed in phosphate-buffered saline (PBS), and cryoprotected in 20% (w/v) sucrose/PBS solution overnight. Hybridization was done overnight at 65°C with RNA probes (300 ng/ml) in hybridization buffer {50% (v/v) formamide, 10% (w/v) dextran sulfate, ribosomal RNA (rRNA; 1 mg/ml), 1× Denhardt's solution, and 1× salt solution [200 mM NaCl, 10 mM tris (pH 7.5), 5 mM sodium phosphate buffer, and 5 mM EDTA]}. Probes were detected with an anti–Dig–alkaline phosphatase (AP) antibody (1:3500; Roche). The AP activity was revealed using 4-nitro blue tetrazolium chloride/5-bromo-4-chloro-3-indolyl-phosphate substrate solution (Roche).

Generation of hBCOR stable cell lines and cell culture conditions

Stable cell lines were generated from Flp-In T-Rex 293 cells (Invitrogen) according to the manufacturer's recommendations. Two micrograms of POG44 vector in combination with 0.5 μg of one of the following vectors, pCDNA5-FRT/TO-*BCOR::EGFP*, pCDNA5-FRT/TO-*BCOR-L685F::EGFP*, pCDNA5-FRT/TO-*BCOR-P483L::EGFP*, pCDNA5-FRT/TO-*BCOR-R856S::EGFP*, pCDNA5-FRT/TO-*BCOR-E1154G::EGFP*, pCDNA5-FRT/TO-*BCOR::BirA-3xFlag*, pCDNA5-FRT/TO-*BCOR-L685F::BirA-3xFlag*, pCDNA5-FRT/TO-*BCOR-P483L::BirA-3xFlag*, pCDNA5-FRT/TO-*BCOR-R856S::BirA-3xFlag*, or pCDNA5-FRT/TO-*BCOR-E1154G::BirA-3xFlag*, was transfected into Flp-In T-Rex 293 cells using jetPRIME Reagent (VRW). Following hygromycin (Thermo Fisher Scientific) selection at 200 μg/ml, unique clones were selected for each genotype. Cells at ~60 to 70% confluence were treated with tetracycline (1 μg/ml) (Millipore-Sigma) for 24 hours to induce protein expression before collection for the different assays used (protein turnover study and BioID).

Protein turnover by flow cytometry

T-Rex 293 tetracycline inducible stable cell lines described above were grown to 70% confluence and treated with tetracycline (1 μg/ml) for 24 hours to induce protein expression. To assess protein stability, cycloheximide (100 μg/ml) was then added to the medium and cells were collected by trypsinization after 0, 2, 4, 6, and 8 hours. Cells were resuspended in a propidium iodide (PI) solution containing 1× PBS, 5 mM EDTA, and PI (10 μg/ml) (Sigma-Aldrich) to exclude dead cells from the analysis. Samples were processed on a FACSCalibur flow cytometer, and acquisition was done using the CellQuest software. Geometric mean fluorescence intensity (Geo MFI) for each of the time points was calculated using FlowJo (*65*). Protein levels were expressed on the basis of the measured fluorescence values using the Geo MFI index method and normalized to $T = 0$.

Immunohistochemistry

Immunohistochemistry was carried out on retinal cryosections using standard procedures. Bound antibodies were detected with appropriate secondary antibodies conjugated to Alexa Fluor 488, 555, or 647 (1:1000; Thermo Fisher Scientific).

See table S12 for the description of the antibodies, concentration used, and fixation details. Note that CRX and OTX2 antibodies cross-recognize both proteins (*66*).

Luciferase assay

P0 mice were sacrificed, and eyes were enucleated. Eyes were injected in the subretinal space with 1 μl of a plasmid DNA mixture and electroporated using CUY650 tweezer electrodes (Protech) and the ECM830 Electroporation System (Harvard Apparatus) with the following settings: 5 pulses, 50 mV, pulse length of 50 ms, and 950-ms intervals with unipolar polarity. Plasmid DNA mixture contains the luciferase reporter plasmid DNAs *pNrl*-luciferase or *pRHO*-luciferase (0.45 μg/μl); shRNA against mouse *Bcor*, pSCV2-*shBcor*, or empty expression vector pSCV2 (0.25 μg/μl); and overexpression vector pCIG2-*Bcor* or empty vector pCIG2 (0.25 μg/μl). pIS2-Renilla luciferase reporter vector (25 ng/μl) driven by the SV40 early enhancer/promoter was cotransfected for normalization of transfection efficiency.

After electroporation, retinas were explanted and cultured for 2 days (*pNrl*-luciferase) or 5 days (*pRHO*-luciferase), as previously described (*67*). Dissociation was done by transferring each explant in a solution of PBS containing papain (15 active units/ml) (Worthington), L-cysteine (0.2 mg/ml) (Sigma-Aldrich), and deoxyribonuclease (DNase) (4 mg/ml) (Worthington) for 5 min at 37°C. The enzymatic reaction was neutralized in a solution of low ovomucoid containing DNase (4 mg/ml), and cells were dissociated by trituration. Cells were collected by centrifugation and lysed in 110 μl of cell lysis buffer [200 mM tris (pH 7.5), 100 mM NaCl, and 0.125% (v/v) Triton X-100].

For promoter assays, HEK 293T [for *pRHO*-luciferase and $(CE3)_3$-POMC-luciferase] or rat fibroblasts [for $(CE3)_3$-POMC-luciferase] cells were plated in a 24-well plate and a plasmid DNA mixture was transfected in each well using jetPRIME Reagent (VWR) or Lipofectamine 3000 (Thermo Fisher Scientific), respectively, following the manufacturer's recommendations. For reporter assay using *pRHO*-luciferase, plasmid DNA mixture contains 350 ng of *pRHO*-luciferase; 150 ng of shRNA against *hBCOR*, pSCV2-*shBCOR*, or scramble *shRNA* vector pSCV2; 150 ng of overexpression vector pCIG2-*Bcor*, truncated form pCIG2-*Bcor*Δ9-10, or empty expression vector pCIG2; and 150 ng of pCDNA3.1-3xFlag::*Crx* or pCIG2-3xFlag::*Otx2* expression vector along with 20 ng of pIS2-Renilla. For reporter assays using $(CE3)_3$-POMC-luciferase, plasmid DNA mixture contains 50 ng of reporter vector, 100 ng of expression vector pCS2-MT-*OTX2* or pCS2-MT empty vector for equal molar ratio of promoter, and between 0 and 250 ng of expression vector pCAGGS-*BCOR*::Flag, pCAGGS-*BCOR-L685F*::Flag, pCAGGS-*BCOR-P483L*::Flag, pCAGGS-*BCOR-R856S*::Flag, or pCAGGS-*BCOR-E1154G*::Flag, pCAGGS-*BCOR*Δ*BCL6*::Flag, or pCIG2-*Bcor*Δ9-10 along with pBlueScript II as DNA filler (for equal DNA quantity in each condition) and pCAGGS empty vector for equal molar ratio of promoter in each condition.

Each condition was done in triplicate. After transfection, cells were incubated for 24 hours at 37°C with 5% CO_2. After incubation, medium was removed and cells in each well were lysed in 110 μl of cell lysis buffer. Samples were frozen at −80°C, allowed to thaw on ice, and homogenized by trituration. One hundred microliters of each sample was loaded in a white 96-well plate.

Luminescence signal was detected using a GloMax 96 Microplate Luminometer detection system (Promega). Firefly luciferase activity was measured by injection of 100 μl of a 2× solution containing 100 mM tris (pH 7.5), 10 mM dithiothreitol (DTT) (ref), 0.4 mM coenzyme A (Santa Cruz Biotechnology), 0.60 mM adenosine triphosphate (ATP) (GoldBio), and D-luciferin (5.6 mg/ml) (GoldBio). The optimal *OTX2* concentration used in the repression assay was determined by fitting an activation curve of the POMC promoter and selecting the concentration that gives 80% activation. The IC_{50} of *wtBCOR* and *mutBCOR* was determined by plotting the best fitting curve on each triplicate using a nonlinear regression curve fit analysis. To be included in the analysis, the R squared of each curve had to be higher than 0.75 (only one curve was excluded because of a low R squared). The IC_{50} was calculated to fall between the top and bottom value of the linear phase of each curve.

NanoBiT assay

NanoBiT assay (Promega) was performed following the manufacturer's recommendation. Briefly, HEK 293T cells were transiently transfected using Lipofectamine 3000 (Thermo Fisher Scientific) with a mixture of pSCV2-*shBCOR* and pBit2.1-TK-SmBit::*Numb65* as a negative control or pBit2.1-TK-SmBit::*BCL6* as a positive control or pBit2.1-TK-SmBit::*NRL* together with pCAGGS-LgBit::*BCOR*. Cells were incubated for 24 hours, and Nano-Glo live cell reagent was added to the medium. Luminescence was read on a Glomax spectrophotometer (Promega).

Immunoprecipitation

P7 to P9 animals were sacrificed, the eyes were enucleated, and the retinas were collected. After cell lysis in NP-40 buffer [50 mM tris (pH 8.0), 150 mM NaCl, 1% (w/v) NP-40, and complete protease inhibitor cocktail (Roche)], samples were centrifuged for 15 min at 15,100*g*. The supernatants were collected, and the total protein concentration was determined using the Bradford protein assay (Bio-Rad).

For in vitro assay, HEK 293T cells were transiently transfected using jetPRIME reagent (VWR) with pCAGGS-3xFlag::*Crx*, pCIG2-3xFlag::*Otx2*, or an empty expression vector pCAGGS-3xFlag together with the overexpression vector pCIG2-*Bcor* or pCIG2-*Bcor*Δ9-10 in fig. S2F or with pCS2-MT-*OTX2* or the empty expression vector pCS2-MT together with the overexpression vector pCAGGS-*BCOR*::Flag wild type (wt) or mutants in fig. S6E. Cells were lysed 24 hours after transfection in NP-40 lysis buffer and centrifuged for 15 min at 15,100*g*. The supernatants were collected, and the total protein concentration was determined using the Bradford protein assay.

Four micrograms of mouse anti-BCOR C-10 antibody (Santa Cruz Biotechnology) was bound to 40 μl of protein G Dynabeads (Thermo Fisher Scientific), according to the manufacturer's recommendations, and incubated with 2 to 3 mg of total proteins overnight at 4°C in IpH 0.1% buffer [50 mM tris (pH 8.0), 150 mM NaCl, 5 mM EDTA, 0.1% (w/v) NP-40, and complete protease inhibitor cocktail (Roche)]. Immunoprecipitated samples were analyzed by Western blotting using homemade 10% acrylamide gel, rapid transfer for mixed protein molecular weight into polyvinylidene difluoride membrane (Tans-Blot system, Bio-Rad), 5% milk blocking, and overnight primary antibody incubation at 4°C. Membranes were then incubated with horseradish peroxidase–conjugated secondary antibodies before final protein visualization using ECL prime (Bio-Rad) or the IRDye secondary antibodies 680RD and 800CW (LI-COR Biosciences). Optimal exposure times were performed using the ChemiDoc system (Bio-Rad) or the Odyssey CLx system (LI-COR Biosciences). Quantification of coIP was performed using ImageLab (Bio-Rad) or Odyssey CLx system (LI-COR Biosciences). Raw signal intensities were first obtained for immunoprecipitated proteins and inputs. Background signal was deducted from each value. Final quantification data were given as the ratio of immunoprecipitated signal to input signal, each value normalized to the wt condition. See table S12 for the description of the antibodies and concentration used.

Pull-down assay

Protein synthesis was induced with the addition of 0.1 mM isopropyl-β-D-thiogalactopyranoside (IPTG) for 3 hours at 37°C. Cells were lysed by sonication with 10 short bursts of 10 s followed by intervals of 30 s for cooling in a solution of PBS + 1% Triton X-100 + complete protease inhibitor (Roche). Cell debris was removed by centrifugation, and glutathione *S*-transferase (GST) protein complex was purified by immobilization onto glutathione agarose beads (Pierce).

T-Rex 293 tetracycline inducible stable cell lines expressing BCOR::EGFP, BCOR-L685F::EGFP, BCOR-P483L::EGFP, BCOR-R856S::EGFP, and BCOR-E1154G::EGFP were grown to 70% confluence and treated with tetracycline (1 μg/ml) for 24 hours to induce protein expression.

Ten micrograms of protein complex (GST::*POZ-BCL6* or *GST* alone) immobilized on glutathione agarose beads and 500 ng of cell lysates were incubated in IpH 0.1% buffer overnight at 4°C. Pulled down samples were analyzed by Western blot.

Immunoprecipitation followed by mass spectrometry (liquid chromatography–MS/MS)

Following immunoprecipitation, samples were washed five times with 50 mM ammonium bicarbonate and resuspended in 50 μl of fresh 50 mM ammonium bicarbonate. The on-bead proteins were diluted in 2 M urea/50 mM ammonium bicarbonate, and trypsin digestion was performed overnight at 37°C. The samples were reduced with 13 mM DTT at 37°C for 30 min and, after cooling for 10 min, alkylated with 23 mM chloroacetamide at room temperature for 20 min in the dark. The supernatants were acidified with trifluoroacetic acid and cleaned from residual detergents and reagents with MCX cartridges (Waters Oasis MCX 96-well Elution Plate) following the manufacturer's recommendations. After elution in 10% ammonium hydroxide/90% methanol (v/v), samples were dried with SpeedVac, reconstituted under agitation for 15 min in 12 μl of 2% acetonitrile (ACN)–1% formic acid (FA), and loaded into a 75-μm inside diameter × 150 mm Self-Pack C18 column installed in the Easy-nLC II system (Proxeon Biosystems). Peptides were eluted with a two-slope gradient at a flow rate of 250 nl/min. Solvent B (0.2% FA in ACN) first increased from 2 to 35% in 105 min and then from 35 to 85% B in 15 min. The high-performance liquid chromatography system was coupled to an Orbitrap Fusion mass spectrometer (Thermo Fisher Scientific) through the Nanospray Flex Ion Source. Nanospray and S-lens voltages were set to 1.3 to 1.7 kV and 50 V, respectively. Capillary temperature was set to 225°C. Full-scan MS survey spectra [mass/charge ratio (*m/z*) 360 to 1560] in profile mode were acquired by the Orbitrap with a resolution of 120,000 with a target value at 3 × 105. The 25 most intense peptide ions were fragmented in the high collision dissociation (HCD) cell and analyzed in the linear ion trap with a target value at 2 × 104 and a normalized collision energy at 28 V. Target ions selected for fragmentation were dynamically excluded for 25 s after two MS/MS events.

The peak list files were generated using Proteome Discoverer program (version 2.3) with the following parameters: minimum mass set to 500 Da, maximum mass set to 6000 Da, no grouping of MS/MS spectra, precursor charge set to auto, and minimum number of fragment ions set to 5. Protein database search was performed using Mascot 2.6 program (Matrix Science) against the UniProt *Mus musculus* protein database (15 April 2015). The mass tolerances for precursor and fragment ions were set to 10 parts per million (ppm) and 0.6 Da, respectively. Data interpretation was performed using Scaffold program (version 4.8).

Data analysis was done on Excel (Microsoft), considering exclusive spectrum counts and applying the following filters: All the hits specific to Bcor IP only were included for monoclonal BCOR antibody samples, and hits with a minimum of five exclusive spectrum counts, enriched fivefold over immunoglobulin G (IgG) control, were considered for polyclonal BCOR antibody. See table S12 for description of the antibodies and concentration used.

BioID (liquid chromatography–MS/MS)

BioID was performed as previously published. The peak list files were generated with Proteome Discoverer program (version 2.3) using the following parameters: minimum mass set to 500 Da, maximum mass set to 6000 Da, no grouping of MS/MS spectra, precursor charge set to auto, and minimum number of fragment ions set to 5. Protein database searching was performed with Mascot 2.6 program (Matrix Science) against the UniProt human protein database (16 May 2018) containing the common contaminant proteins usually observed in BioID samples. The mass tolerances for precursor and fragment ions were set to 10 ppm and 0.6 Da, respectively. Trypsin was used as the enzyme allowing for up to one missed cleavage. Cysteine carbamidomethylation was specified as a fixed modification, and methionine oxidation and ubiquitylation on lysine were specified as variable modifications. Data interpretation was performed using Scaffold program (version 4.8).

MS/MS raw data were searched against the UniProt database (downloaded on 26 March 2019) using MaxQuant program (version 1.6.6.0) for protein identification and label-free quantifications (LFQs). LFQs were transferred in Perseus program (version 1.6.10.43). Proteins that MaxQuant flagged as being identified only by site, reverse, or potential contaminant were removed from the analysis. Samples were clustered using the Hierarchical clustering algorithm from Perseus with the default settings. Only the samples that clustered with their largest group were kept for further analysis. This resulted in four samples kept for BCOR and two samples kept for L685F, P483L, BCORΔBCL6, R856S, and E1154G mutants. Proteins quantified in two of four samples for BCOR or in two of two samples for L685F, P483L, BCORΔBCL6, R856S, and E1154G mutants were kept for further analysis. LFQs reported as 0 by MaxQuant were replaced by randomly generated values normally distributed with a mean downshifted by 1.8 and SD equal to 0.3 compared to non-0 LFQs of their respective sample. BCOR, L685F, P483L, BCORΔBCL6, R856S, and E1154G proteins were compared to BirA alone, GFP, NLS (nuclear localization signal), and GFP-NLS control samples using a two-tailed *t* test subsequently adjusted for multiple hypothesis testing using a permutation-based test by considering a false discovery rate (FDR) of 10% adjusted using an s0 correction factor of 0.1 with 10,000 iterations. Proteins were labeled as high-confidence interactors when their FDR value was under 0.1 and their LFQ ratio was over 2 against all control groups. *Z*-score intensities of wt and mutants were computed for each individual genes. Euclidean clustering was computed on the genes and the individual samples based on the *z* scores. Statistical differences between the raw (non–*z*-scored) LFQs of BCOR against L685F, P483L, BCORΔBCL6, R856S, and E1154G were determined using a two-tailed *t* test subsequently adjusted for multiple hypothesis testing using a permutation-based test by considering an FDR of 5% adjusted using an s0 correction factor of 0.1 with 10,000 iterations. The level of differential interaction with BCOR was considered statistically significant when the adjusted *P* value was <0.05.

Proximity ligation assay

Tissues were prepared and sectioned as mentioned above. Slides were preincubated in blocking solution for 30 min and incubated with a mixture of the following antibodies diluted in blocking solution: rabbit anti-BCOR [RRID:AB_2716801 (*21*)] alone or BCOR with mouse anti-CRX (Novus Biologicals), goat anti-OTX2 (R&D Systems), or mouse anti-PKCα H-7 (Santa Cruz Biotechnology). Duolink PLA fluorescence (Sigma-Aldrich) reaction was done according to the manufacturer's recommendations.

Quantitative RT-PCR

In vivo electroporation of P0 eyes was performed as described previously (*63*) using plasmid DNA at 1 μg/μl [pSCV2-*shBcor* (*33*), pCIG2-*Bcor*, or empty vector pSCV2, pCIG2 as control]. The electroporated eyes were collected at P2 and P7, retinas were dissected out, and cells were dissociated in papain. GFP-expressing cells were collected by fluorescence-activated cell sorting (FACS) directly in RNeasy lysis tissue (RLT) buffer (Qiagen), RNA was isolated using the RNeasy Micro Kit (Qiagen), and first-strand cDNA was prepared using a SuperScript IV VILO cDNA synthesis kit (Thermo Fisher Scientific) each following the manufacturer's recommendations.

qRT-PCRs were set up using a mixture of 15 to 150 pg of total cDNA template, 0.3 μM of both primers (forward and reverse), and 1× PowerUp SYBR green master mix (Thermo Fisher Scientific). The reaction was carried out using the Applied Biosystems ViiA7 real-time PCR machine using the following settings: 2 min at 95°C for one cycle, 15 s at 95°C, then 1 min at 60°C for 40 cycles. A dissociation curve for each primer set was done after each PCR with the following settings: 15 s at 95°C, 1 min at 60°C, and 15 s at 95°C. *Gapdh* was used as a reference gene for normalization. Data analysis was performed using QuantStudio software and presented as relative quantification, normalized to one of the control samples. See table S10 for primer sequences.

RNA sequencing

Two litters of P0 CD1 mice eyes were electroporated as described previously (*63*) using plasmid DNA at 1 μg/μl (pSCV2-*shBcor* or empty vector pSCV2 as control). The electroporated eyes were collected at P21 and processed for dissection, dissociation, FACS sorting, RNA extraction (RNeasy Mini kit, Qiagen), and reverse transcription as described above in the qPCR section with minor modifications. (i) Dissociation was done with StemPro Accutase (Thermo Fisher Scientific) for 30 min instead of papain, and (ii) cells were treated with PI solution before sorting. Cells (10 to 15%) were excluded because of cell death. GFP^+ cells were sorted directly into lysis buffer. Multiple sorted GFP^+ cell samples were combined to obtain 30,000 to 70,000 cells per replicate (n = 2) and purified using the RNeasy Mini kit (Qiagen).

Sample quantity (RNA integrity number) and quality were assessed using the Agilent RNA 6000 Pico Kit (Agilent, #5067-1513) on Bioanalyzer 2100. Library preparation started with rRNA depletion using the Ribo-Zero Magnetic Gold Kit (Human/Mouse/Rat) (Epicentre for Illumina #MRZG12324). Total RNA (3.0 to 5.1 ng) was used for rRNA depletion of the total RNA. SpeedVac sublimation was performed on some samples to reduce RNA volume to 17 μl to start the depletion reaction. rRNA-depleted RNA was then purified with the AGENCOURT RNA CLEAN XP Kit (Beckman Coulter). The samples were eluted in 8.5 μl of H_2O to continue the library preparation using the SMARTer Stranded RNA-Seq Kit (Takara Bio USA Inc., #634836 or #634837). For this protocol, the first-strand synthesis was performed using a modified N6 primer (the SMART Stranded N6 Primer) to obtain full-length fragments. The full-length, single-stranded cDNA fragments were purified with the Agencourt DNA CleanUp AMPure XP Kit (Beckman Coulter, #A63881). PCR enrichment + indexing step of 15 cycles was then performed using the Illumina Indexing Primer Set provided by the kit. The final enriched product (library, after PCR) was purified using the Agencourt DNA CleanUp AMPure XP Kit (Beckman Coulter, #A63881). Libraries were eluted in 16 μl of elution buffer. Quality and quantification of the libraries were assessed using the Agilent High Sensitivity DNA Kit (Agilent, #5067-4626) on Bioanalyzer 2100. The libraries were then quantified by qPCR to obtain their nanomolar concentration. Libraries were diluted and pooled equimolar before paired-end sequencing performed with 50 cycles (PE50) on a v4 flowcell (Illumina, HiSeq PE Cluster Kit v4 cBot, PE-401-4001) of the Illumina HiSeq 2500 System.

See table S13 for detailed library parameters per sample. See also Supplementary Text for details on RNA-seq data analysis.

CUT&RUN sequencing

C&R experiments were performed as described previously (*42*), with a few modifications. The entire procedure was done in 200-μl PCR tubes. Final digitonin concentration was set at 0.01%. pAG-MNase (internal production from a plasmid obtained from S. Henikoff) digestion was performed for 30 min on ice.

Libraries were prepared with the KAPA DNA HyperPrep Kit (Roche, 07962363001-KK8504). This protocol includes an end-repair/A-tailing step and an adapter ligation step followed by a PCR amplification (enrichment) of ligated fragments. See table S14 for detailed PCR cycles per sample. The adapters used for ligation were IDT for Illumina TruSeq UD Indexes (Illumina, 20022371). The final enriched product (library, after PCR) was purified using KAPA purification beads (Roche, 07983298001-KK8002), and double size selection (SPRIselect, Beckman Coulter) was performed (with KAPA beads) to select fragments between 180 and 500 bp.

Libraries were then quantified using a NanoDrop microvolume spectrophotometer (ng/μl), and quality was assessed using the Agilent High Sensitivity DNA Kit (Agilent, 5067-4626) on Bioanalyzer 2100. The libraries were then quantified by qPCR to obtain their nanomolar concentration. Libraries were diluted, pooled equimolar, and sequenced in PE50 on an S1 flowcell (Illumina, 20012863) of the Illumina NovaSeq 6000 System.

See Supplementary Text for details on C&R data analysis.

Human scRNA-seq published dataset analysis

Raw reads were downloaded from ArrayExpress under accession number E-MTAB-7316 (*32*). Cell Ranger count was used to generate gene expression matrix file for further analysis. SCANPY was used to generate the Uniform Manifold Approximation and Projection (UMAP) plots (*68*).

Patients

All human protocols were reviewed and approved by the participating university centers, and informed consent was obtained from all subjects involved in this study. We studied patients from five distinct families (Fig. 6B) originating from France and Canada (one), China (three), and the United States (one). Despite differences in the severity of symptoms, all patients presented with the same early childhood onset retinal degeneration, which was first observed in

males only, and were diagnosed with a possible X-linked RP. Patients developed early visual acuity loss and night blindness, followed by visual field loss and variable but severe atrophic retinal changes (Fig. 6A), loss of retinal architecture, severe retinal thinning, loss of autofluorescence, and loss of ERG signals. Both rod and cone signals became undetectable in most of the cases (Table 1 and fig. S5). The X-linked RP, diagnosed in all five families, eventually progressed to complete blindness (no light perception) for male patients, while females showed variable expressivity with symptoms ranging from unaffected (most of the female family members, not specific description) to severe (patient IV-2).

Whole-exome sequencing

Blueprint genetic testing on E1154G proband 3072 (250+ known IRD genes) was negative, further indicating that no known mutations were missed while first screening these patients and motivated the WES analysis for this family. Library preparation and WES were performed at the Genome Quebec and McGill Applied Genomics Innovation Core (MAGIC) for two affected siblings from the French-Canadian family I and their mother (Fig. 6B). Target capture was performed with the SureSelect All Exon 50 MB (V5) exome enrichment Kit (Agilent) following the manufacturer's recommendations. A multiplex approach with molecular barcodes for traceable identification of samples was used. Sequencing was carried out with Illumina HiSeq 2000, and 100-bp paired-end reads were generated. The barcode sequences were removed, and reads were quality-trimmed using the Fastx toolkit 0.11.2 (http://hannonlab.cshl.edu/fastx_toolkit/). Reads were mapped to hg19 with BWA 0.7.7 (*69*), and indel realignment and base recalibration were done using GATK 3.1-1 (*70*). Picard 1.108 (http://picard.sourceforge.net/) was used to mark duplicate reads and exclude them from subsequent analyses. Assessed by GATK, the average mean read depths of bases in consensus coding sequence (CCDS) exons was 83× for these three samples. Average CCDS bases covered by at least 5, 10, and 20 reads were 97.5, 96.4, and 92.8%, respectively.

Single-nucleotide variants (SNVs) and short indels were called using SAMtools 1.2 and BCFtools 1.2 (*71*) with the extended base alignment quality (BAQ) adjustment (–E), and subsequently quality-filtered to require at least 20% of reads supporting the variant call. Further variants were annotated using Annovar (*72*) and our custom scripts. Comparison of variants was done against dbSNP138, EVS, 1000 genomes dataset, ExAC data, and our internal database (approximately 3000 exomes previously sequenced at our center) to exclude any common single-nucleotide polymorphisms. Variants seen in more than 10 control exomes were excluded from further analysis. Only variants predicted to change protein sequence (exonic nonsynonymous SNVs, short indels, and splice site SNVs) were further considered. Validation studies and sequencing were performed at MAGIC by regular Sanger sequencing using the ABI 3730XL instrument (Thermo Fisher Scientific).

In silico analyses

To evaluate the potential damage of the six *BCOR* mutations on protein structure and function, to evaluate their affected nucleotide's conservation across the animal kingdom, and to assess the frequency in normal human populations, we performed the following studies. To assess pathogenicity of our mutations, we used and calculated CADD, SIFT, PolyPhen-2, and MutationTaster. CADD calculated the deleteriousness score of SNVs, where scores >15 are considered severely deleterious. SIFT amino acid substitutions calculate the phenotypic effect of mutations, and scores range from 0.0 (deleterious) to 1.0 (tolerated). PolyPhen-2 is a tool that predicts the impact of an amino acid substitution on the structure and function of a human protein and ranges from 0 to 1. Unlike SIFT, the closer to 1, the more severe. MutationTaster is a substitution tool, where a value close to 1 indicates a high "security" that the change is deleterious. For normal populations, we used four databases: ExAC, EVS, 1KGP, or our own internal control databases.

For conservation assessments and calculations, we used the following three methods: GERP, PhyloP-100, and nucleotide alignments through the animal kingdom (Fig. 6D). The GERP score measures evolutionary conservation, and scores >4 are significant. PhyloP-100 scores measure evolutionary conservation at individual alignment sites compared to the evolution that is expected under neutral drift. Positive PhyloP-100 scores indicate slower evolution, and negative scores indicate faster evolution compared to neutral drift. Figure 6D illustrates the amino acid alignments of our mutant protein sequences through the animal kingdom, down to the amphibian *Xenopus tropicalis*.

Quantifications of cell types and analysis of electroporated retinas

At least three different images were counted per animal. Quantification of bipolar and photoreceptor cells in Bcor animals was done using a homemade automated program on ImageJ. Quantification of the percentage of GFP^+ cells in the ONL after *wtBCOR* and mutant misexpression at P60 was done using a homemade automated program on ImageJ. For Müller cell body surface measurements, GFP^+/$LHX2^+$ cell body was traced using the freehand tool and cell size was calculated using the area value of each selected cell with ImageJ. The scale was calibrated in micrometers. A minimum of three independent images was used to generate cell counts and Müller cell body surface measurements.

For analysis of degeneration following BCOR mutant expression, we used a semiquantitative degeneration index, defined as follows: Stage 1 represents normal changes observed after electroporation (rare rosettes and injection site visible); stage 2 represents slightly disorganized retina and layering with increased rosette frequency; stage 3 represents multiple area with rosettes, disorganized layers, and thinner photoreceptor layer; and stage 4 represents severe degeneration with rosettes, disorganized layers, and low to no photoreceptors.

Statistical analysis

Statistical analysis was carried out using Prism software (GraphPad). For each condition shown, averaged values from a specified minimum of biological replicates from independent cultures or animals were calculated and the resulting SD or SEM was reported in the error bars. Unless otherwise specified, for each experiment, averaged values for each sample were compared to that of the GFP control, wt, or littermates corresponding to control genotype and the significance was calculated using one- or two-way analysis of variance (ANOVA) with the Dunnett or Tukey test correction for datasets with single or multiple conditions, respectively, or multiple *t* test for datasets with only two conditions.

SUPPLEMENTARY MATERIALS

Supplementary material for this article is available at https://science.org/doi/10.1126/sciadv.abh2868

View/request a protocol for this paper from *Bio-protocol*.

REFERENCES AND NOTES

1. S. P. Daiger, L. S. Sullivan, S. J. Bowne, Genes and mutations causing retinitis pigmentosa. *Clin. Genet.* **84**, 132–141 (2013).
2. J. A. Brzezinski, T. A. Reh, Photoreceptor cell fate specification in vertebrates. *Development* **142**, 3263–3273 (2015).
3. A. Swaroop, D. Kim, D. Forrest, Transcriptional regulation of photoreceptor development and homeostasis in the mammalian retina. *Nat. Rev. Neurosci.* **11**, 563–576 (2010).
4. A. Nishida, A. Furukawa, C. Koike, Y. Tano, S. Aizawa, I. Matsuo, T. Furukawa, Otx2 homeobox gene controls retinal photoreceptor cell fate and pineal gland development. *Nat. Neurosci.* **6**, 1255–1263 (2003).
5. J. C. Corbo, K. A. Lawrence, M. Karlstetter, C. A. Myers, M. Abdelaziz, W. Dirkes, K. Weigelt, M. Seifert, V. Benes, L. G. Fritsche, B. H. F. Weber, T. Langmann, CRX ChIP-seq reveals the cis-regulatory architecture of mouse photoreceptors. *Genome Res.* **20**, 1512–1525 (2010).
6. M. Housset, A. Samuel, M. Ettaiche, A. Bemelmans, F. Beby, N. Billon, T. Lamonerie, Loss of Otx2 in the adult retina disrupts retinal pigment epithelium function, causing photoreceptor degeneration. *J. Neurosci.* **33**, 9890–9904 (2013).
7. A. Samuel, M. Housset, B. Fant, T. Lamonerie, Otx2 ChIP-seq reveals unique and redundant functions in the mature mouse retina. *PLOS ONE* **9**, e89110 (2014).
8. H. Yamamoto, T. Kon, Y. Omori, T. Furukawa, Functional and evolutionary diversification of Otx2 and Crx in vertebrate retinal photoreceptor and bipolar cell development. *Cell Rep.* **30**, 658–671.e5 (2020).
9. S. Sato, T. Inoue, K. Terada, I. Matsuo, S. Aizawa, Y. Tano, T. Fujikado, T. Furukawa, Dkk3-Cre BAC transgenic mouse line: A tool for highly efficient gene deletion in retinal progenitor cells. *Genesis* **45**, 502–507 (2007).
10. T. Furukawa, E. M. Morrow, T. Li, F. C. Davis, C. L. Cepko, Retinopathy and attenuated circadian entrainment in Crx-deficient mice. *Nat. Genet.* **23**, 466–470 (1999).
11. J. C. Corbo, C. A. Myers, K. A. Lawrence, A. P. Jadhav, C. L. Cepko, A typology of photoreceptor gene expression patterns in the mouse. *Proc. Natl. Acad. Sci. U.S.A.* **104**, 12069–12074 (2007).
12. J. Lee, C. A. Myers, N. Williams, M. Abdelaziz, J. C. Corbo, Quantitative fine-tuning of photoreceptor cis-regulatory elements through affinity modulation of transcription factor binding sites. *Gene Ther.* **17**, 1390–1399 (2010).
13. A. J. Mears, M. Kondo, P. K. Swain, Y. Takada, R. A. Bush, T. L. Saunders, P. A. Sieving, A. Swaroop, Nrl is required for rod photoreceptor development. *Nat. Genet.* **29**, 447–452 (2001).
14. K. P. Mitton, P. K. Swain, S. Chen, S. Xu, D. J. Zack, A. Swaroop, The leucine zipper of NRL interacts with the CRX homeodomain. A possible mechanism of transcriptional synergy in rhodopsin regulation. *J. Biol. Chem.* **275**, 29794–29799 (2000).
15. S. K. Verbakel, R. A. C. van Huet, C. J. F. Boon, A. I. den Hollander, R. W. J. Collin, C. C. W. Klaver, C. B. Hoyng, R. Roepman, B. J. Klevering, Non-syndromic retinitis pigmentosa. *Prog. Retin. Eye Res.* **66**, 157–186 (2018).
16. M. M. Humphries, D. Rancourt, G. J. Farrar, P. Kenna, M. Hazel, R. A. Bush, P. A. Sieving, D. M. Sheils, N. McNally, P. Creighton, A. Erven, A. Boros, K. Gulya, M. R. Capecchi, P. Humphries, Retinopathy induced in mice by targeted disruption of the rhodopsin gene. *Nat. Genet.* **15**, 216–219 (1997).
17. J. Lem, N. V. Krasnoperova, P. D. Calvert, B. Kosaras, D. A. Cameron, M. Nicolò, C. L. Makino, R. L. Sidman, Morphological, physiological, and biochemical changes in rhodopsin knockout mice. *Proc. Natl. Acad. Sci. U.S.A.* **96**, 736–741 (1999).
18. C. L. Makino, X. H. Wen, N. A. Michaud, H. I. Covington, E. DiBenedetto, H. E. Hamm, J. Lem, G. Caruso, Rhodopsin expression level affects rod outer segment morphology and photoresponse kinetics. *PLOS ONE* **7**, e37832 (2012).
19. E. Tan, Q. Wang, A. B. Quiambao, X. Xu, N. M. Qtaishat, N. S. Peachey, J. Lem, S. J. Fliesler, D. R. Pepperberg, M. I. Naash, M. R. al-Ubaidi, The relationship between opsin overexpression and photoreceptor degeneration. *Invest. Ophthalmol. Vis. Sci.* **42**, 589–600 (2001).
20. K. D. Huynh, W. Fischle, E. Verdin, V. J. Bardwell, BCoR, a novel corepressor involved in BCL-6 repression. *Genes Dev.* **14**, 1810–1823 (2000).
21. M. D. Gearhart, C. M. Corcoran, J. A. Wamstad, V. J. Bardwell, Polycomb group and SCF ubiquitin ligases are found in a novel BCOR complex that is recruited to BCL6 targets. *Mol. Cell. Biol.* **26**, 6880–6889 (2006).
22. E. Hilton, J. Johnston, S. Whalen, N. Okamoto, Y. Hatsukawa, J. Nishio, H. Kohara, Y. Hirano, S. Mizuno, C. Torii, K. Kosaki, S. Manouvrier, O. Boute, R. Perveen, C. Law, A. Moore, D. Fitzpatrick, J. Lemke, F. Fellmann, F. G. Debray, F. Dastot-le-Moal, M. Gerard, J. Martin, P. Bitoun, M. Goossens, A. Verloes, A. Schinzel, D. Bartholdi, T. Bardakjian, B. Hay, K. Jenny, K. Johnston, M. Lyons, J. W. Belmont, L. G. Biesecker, I. Giurgea, G. Black, BCOR analysis in patients with OFCD and Lenz microphthalmia syndromes, mental retardation with ocular anomalies, and cardiac laterality defects. *Eur. J. Hum. Genet.* **17**, 1325–1335 (2009).
23. D. Ng, N. Thakker, C. M. Corcoran, D. Donnai, R. Perveen, A. Schneider, D. W. Hadley, C. Tifft, L. Zhang, A. O. M. Wilkie, J. J. van der Smagt, R. J. Gorlin, S. M. Burgess, V. J. Bardwell, G. C. M. Black, L. G. Biesecker, Oculofaciocardiodental and Lenz microphthalmia syndromes result from distinct classes of mutations in BCOR. *Nat. Genet.* **36**, 411–416 (2004).
24. N. Ragge, B. Isidor, P. Bitoun, S. Odent, I. Giurgea, B. Cogné, W. Deb, M. Vincent, J. L. Gall, J. Morton, D. Lim; DDD Study, G. L. Meur, C. Z. Seco, D. Zafeiropoulou, D. Bax, P. Zwijnenburg, A. Arteche, S. T. Swafiri, R. Cleaver, M. M. Entagart, U. Kini, W. Newman, C. Ayuso, M. Corton, Y. Herenger, M. Jeanne, P. Calvas, N. Chassaing, Expanding the phenotype of the X-linked BCOR microphthalmia syndromes. *Hum. Genet.* **138**, 1051–1069 (2019).
25. B. J. Cox, M. Vollmer, O. Tamplin, M. Lu, S. Biechele, M. Gertsenstein, C. van Campenhout, T. Floss, R. Kühn, W. Wurst, H. Lickert, J. Rossant, Phenotypic annotation of the mouse X chromosome. *Genome Res.* **20**, 1154–1164 (2010).
26. M. Y. Hamline, C. M. Corcoran, J. A. Wamstad, I. Miletich, J. Feng, J. L. Lohr, M. Hemberger, P. T. Sharpe, M. D. Gearhart, V. J. Bardwell, OFCD syndrome and extraembryonic defects are revealed by conditional mutation of the Polycomb-group repressive complex 1.1 (PRC1.1) gene BCOR. *Dev. Biol.* **468**, 110–132 (2020).
27. B. S. Clark, G. L. Stein-O'Brien, F. Shiau, G. H. Cannon, E. Davis-Marcisak, T. Sherman, C. P. Santiago, T. V. Hoang, F. Rajaii, R. E. James-Esposito, R. M. Gronostajski, E. J. Fertig, L. A. Goff, S. Blackshaw, Single-cell RNA-seq analysis of retinal development identifies NFI factors as regulating mitotic exit and late-born cell specification. *Neuron* **102**, 1111–1126. e5 (2019).
28. A. Hoshino, R. Ratnapriya, M. J. Brooks, V. Chaitankar, M. S. Wilken, C. Zhang, M. R. Starostik, L. Gieser, A. L. Torre, M. Nishio, O. Bates, A. Walton, O. Bermingham-McDonogh, I. A. Glass, R. O. L. Wong, A. Swaroop, T. A. Reh, Molecular anatomy of the developing human retina. *Dev. Cell* **43**, 763–779.e4 (2017).
29. J. A. Wamstad, V. J. Bardwell, Characterization of Bcor expression in mouse development. *Gene Expr. Patterns* **7**, 550–557 (2007).
30. C. Kizilyaprak, D. Spehner, D. Devys, P. Schultz, In vivo chromatin organization of mouse rod photoreceptors correlates with histone modifications. *PLOS ONE* **5**, e11039 (2010).
31. I. Solovei, M. Kreysing, C. Lanctôt, S. Kösem, L. Peichl, T. Cremer, J. Guck, B. Joffe, Nuclear architecture of rod photoreceptor cells adapts to vision in mammalian evolution. *Cell* **137**, 356–368 (2009).
32. S. W. Lukowski, C. Y. Lo, A. A. Sharov, Q. Nguyen, L. Fang, S. S. Hung, L. Zhu, T. Zhang, U. Grünert, T. Nguyen, A. Senabouth, J. S. Jabbari, E. Welby, J. C. Sowden, H. S. Waugh, A. Mackey, G. Pollock, T. D. Lamb, P.-Y. Wang, A. W. Hewitt, M. C. Gillies, J. E. Powell, R. C. Wong, A single-cell transcriptome atlas of the adult human retina. *EMBO J.* **38**, e100811 (2019).
33. L. Tiberi, J. Bonnefont, J. van den Ameele, S.-D. le Bon, A. Herpoel, A. Bilheu, B. W. Baron, P. Vanderhaeghen, A BCL6/BCOR/SIRT1 complex triggers neurogenesis and suppresses medulloblastoma by repressing Sonic Hedgehog signaling. *Cancer Cell* **26**, 797–812 (2014).
34. J. E. Roger, A. Hiriyanna, N. Gotoh, H. Hao, D. F. Cheng, R. Ratnapriya, M. A. I. Kautzmann, B. Chang, A. Swaroop, OTX2 loss causes rod differentiation defect in CRX-associated congenital blindness. *J. Clin. Invest.* **124**, 631–643 (2014).
35. T. H.-C. Hsiau, C. Diaconu, C. A. Myers, J. Lee, C. L. Cepko, J. C. Corbo, The *cis*-regulatory logic of the mammalian photoreceptor transcriptional network. *PLOS ONE* **2**, e643 (2007).
36. Z. Wang, M. D. Gearhart, Y.-W. Lee, I. Kumar, B. Ramazanov, Y. Zhang, C. Hernandez, A. Y. Lu, N. Neuenkirchen, J. Deng, J. Jin, Y. Kluger, T. A. Neubert, V. J. Bardwell, N. B. Ivanova, A non-canonical BCOR-PRC1.1 complex represses differentiation programs in human ESCs. *Cell Stem Cell* **22**, 235–251.e9 (2018).
37. Y. Isshiki, A. Iwama, Emerging role of noncanonical polycomb repressive complexes in normal and malignant hematopoiesis. *Exp. Hematol.* **68**, 10–14 (2018).
38. L. M. Kutscher, K. Okonechnikov, N. V. Batora, J. Clark, P. B. G. Silva, M. Vouri, S. van Rijn, L. Sieber, B. Statz, M. D. Gearhart, R. Shiraishi, N. Mack, B. A. Orr, A. Korshunov, B. L. Gudenas, K. S. Smith, A. L. Mercier, O. Ayrault, M. Hoshino, M. Kool, K. von Hoff, N. Graf, G. Fleischhack, V. J. Bardwell, S. M. Pfister, P. A. Northcott, D. Kawauchi, Functional loss of a noncanonical BCOR-PRC1.1 complex accelerates SHH-driven medulloblastoma formation. *Genes Dev.* **34**, 1161–1176 (2020).
39. T. Marquardt, R. Ashery-Padan, N. Andrejewski, R. Scardigli, F. Guillemot, P. Gruss, Pax6 is required for the multipotent state of retinal progenitor cells. *Cell* **105**, 43–55 (2001).
40. S. Wang, C. Sengel, M. M. Emerson, C. L. Cepko, A gene regulatory network controls the binary fate decision of rod and bipolar cells in the vertebrate retina. *Dev. Cell* **30**, 513–527 (2014).
41. T. Lamonerie, J. J. Tremblay, C. Lanctôt, M. Therrien, Y. Gauthier, J. Drouin, Ptx1, a bicoid-related homeo box transcription factor involved in transcription of the pro-opiomelanocortin gene. *Genes Dev.* **10**, 1284–1295 (1996).
42. P. J. Skene, J. G. Henikoff, S. Henikoff, Targeted in situ genome-wide profiling with high efficiency for low cell numbers. *Nat. Protoc.* **13**, 1006–1019 (2018).
43. J. W. Kim, H.-J. Yang, M. J. Brooks, L. Zelinger, G. Karakülah, N. Gotoh, A. Boleda, L. Gieser, F. Giuste, D. T. Whitaker, A. Walton, R. Villasmil, J. J. Barb, P. J. Munson, K. D. Kaya, V. Chaitankar, T. Cogliati, A. Swaroop, NRL-regulated transcriptome dynamics of developing rod photoreceptors. *Cell Rep.* **17**, 2460–2473 (2016).

44. I. Aldiri, B. Xu, L. Wang, X. Chen, D. Hiler, L. Griffiths, M. Valentine, A. Shirinifard, S. Thiagarajan, A. Sablauer, M.-E. Barabas, J. Zhang, D. Johnson, S. Frase, X. Zhou, J. Easton, J. Zhang, E. R. Mardis, R. K. Wilson, J. R. Downing, M. A. Dyer; St. Jude Children's Research Hospital—Washington University Pediatric Cancer Genome Project, The dynamic epigenetic landscape of the retina during development, reprogramming, and tumorigenesis. *Neuron* **94**, 550–568.e10 (2017).
45. T. Tanaka, Y. Nakajima-Takagi, K. Aoyama, S. Tara, M. Oshima, A. Saraya, S. Koide, S. Si, I. Manabe, M. Sanada, M. Nakayama, M. Masuko, H. Sone, H. Koseki, A. Iwama, Internal deletion of BCOR reveals a tumor suppressor function for BCOR in T lymphocyte malignancies. *J. Exp. Med.* **214**, 2901–2913 (2017).
46. J. A. Wamstad, C. M. Corcoran, A. M. Keating, V. J. Bardwell, Role of the transcriptional corepressor Bcor in embryonic stem cell differentiation and early embryonic development. *PLOS ONE* **3**, e2814 (2008).
47. M. Kircher, D. M. Witten, P. Jain, B. J. O'Roak, G. M. Cooper, J. Shendure, A general framework for estimating the relative pathogenicity of human genetic variants. *Nat. Genet.* **46**, 310–315 (2014).
48. P. Kumar, S. Henikoff, P. C. Ng, Predicting the effects of coding non-synonymous variants on protein function using the SIFT algorithm. *Nat. Protoc.* **4**, 1073–1081 (2009).
49. I. A. Adzhubei, S. Schmidt, L. Peshkin, V. E. Ramensky, A. Gerasimova, P. Bork, A. S. Kondrashov, S. R. Sunyaev, A method and server for predicting damaging missense mutations. *Nat. Methods* **7**, 248–249 (2010).
50. J. M. Schwarz, C. Rodelsperger, M. Schuelke, D. Seelow, MutationTaster evaluates disease-causing potential of sequence alterations. *Nat. Methods* **7**, 575–576 (2010).
51. C. Grimm, A. Wenzel, F. Hafezi, S. Yu, T. M. Redmond, C. E. Remé, Protection of Rpe65-deficient mice identifies rhodopsin as a mediator of light-induced retinal degeneration. *Nat. Genet.* **25**, 63–66 (2000).
52. B. A. Price, I. M. Sandoval, F. Chan, R. Nichols, R. Roman-Sanchez, T. G. Wensel, J. H. Wilson, Rhodopsin gene expression determines rod outer segment size and rod cell resistance to a dominant-negative neurodegeneration mutant. *PLOS ONE* **7**, e49889 (2012).
53. T. Rakshit, P. S. Park, Impact of reduced rhodopsin expression on the structure of rod outer segment disc membranes. *Biochemistry* **54**, 2885–2894 (2015).
54. X. H. Wen, L. Shen, R. S. Brush, N. Michaud, M. R. al-Ubaidi, V. V. Gurevich, H. E. Hamm, J. Lem, E. DiBenedetto, R. E. Anderson, C. L. Makino, Overexpression of rhodopsin alters the structure and photoresponse of rod photoreceptors. *Biophys. J.* **96**, 939–950 (2009).
55. D. Athanasiou, M. Aguila, J. Bellingham, W. Li, C. McCulley, P. J. Reeves, M. E. Cheetham, The molecular and cellular basis of rhodopsin retinitis pigmentosa reveals potential strategies for therapy. *Prog. Retin. Eye Res.* **62**, 1–23 (2018).
56. E. Z. Macosko, A. Basu, R. Satija, J. Nemesh, K. Shekhar, M. Goldman, I. Tirosh, A. R. Bialas, N. Kamitaki, E. M. Martersteck, J. J. Trombetta, D. A. Weitz, J. R. Sanes, A. K. Shalek, A. Regev, S. A. McCarroll, Highly parallel genome-wide expression profiling of individual cells using nanoliter droplets. *Cell* **161**, 1202–1214 (2015).
57. A. Barabino, V. Plamondon, M. Abdouh, W. Chatoo, A. Flamier, R. Hanna, S. Zhou, N. Motoyama, M. Hébert, J. Lavoie, G. Bernier, Loss of Bmi1 causes anomalies in retinal development and degeneration of cone photoreceptors. *Development* **143**, 1571–1584 (2016).
58. N. Fujimura, A. Kuzelova, A. Ebert, H. Strnad, J. Lachova, O. Machon, M. Busslinger, Z. Kozmik, Polycomb repression complex 2 is required for the maintenance of retinal progenitor cells and balanced retinal differentiation. *Dev. Biol.* **433**, 47–60 (2018).
59. Y. Omori, S. Kubo, T. Kon, M. Furuhashi, H. Narita, T. Kominami, A. Ueno, R. Tsutsumi, T. Chaya, H. Yamamoto, I. Suetake, S. Ueno, H. Koseki, A. Nakagawa, T. Furukawa, Samd7 is a cell type-specific PRC1 component essential for establishing retinal rod photoreceptor identity. *Proc. Natl. Acad. Sci. U.S.A.* **114**, E8264–E8273 (2017).
60. S. J. Wong, M. D. Gearhart, A. B. Taylor, D. R. Nanyes, D. J. Ha, A. K. Robinson, J. A. Artigas, O. J. Lee, B. Demeler, P. J. Hart, V. J. Bardwell, C. A. Kim, KDM2B recruitment of the polycomb group complex, PRC1.1, requires cooperation between PCGF1 and BCORL1. *Structure* **24**, 1795–1801 (2016).
61. A. Astolfi, M. Fiore, F. Melchionda, V. Indio, S. N. Bertuccio, A. Pession, BCOR involvement in cancer. *Epigenomics* **11**, 835–855 (2019).
62. M. J. Mattapallil, E. F. Wawrousek, C.-C. Chan, H. Zhao, J. Roychoudhury, T. A. Ferguson, R. R. Caspi, The Rd8 mutation of the Crb1 gene is present in vendor lines of C57BL/6N mice and embryonic stem cells, and confounds ocular induced mutant phenotypes. *Invest. Ophthalmol. Vis. Sci.* **53**, 2921–2927 (2012).
63. J. de Melo, S. Blackshaw, In vivo electroporation of developing mouse retina. *J. Vis. Exp.*, 2847 (2011).
64. M. Cayouette, B. A. Barres, M. Raff, Importance of intrinsic mechanisms in cell fate decisions in the developing rat retina. *Neuron* **40**, 897–904 (2003).
65. S. A. Comyn, T. Mayor, A method to monitor protein turnover by flow cytometry and to screen for factors that control degradation by fluorescence-activated cell sorting. *Methods Mol. Biol.* **1844**, 137–153 (2018).
66. N. Fossat, C. le Greneur, F. Béby, S. Vincent, P. Godement, G. Chatelain, T. Lamonerie, A new GFP-tagged line reveals unexpected Otx2 protein localization in retinal photoreceptors. *BMC Dev. Biol.* **7**, 122 (2007).
67. J. Elliott, C. Jolicoeur, V. Ramamurthy, M. Cayouette, Ikaros confers early temporal competence to mouse retinal progenitor cells. *Neuron* **60**, 26–39 (2008).
68. F. A. Wolf, P. Angerer, F. J. Theis, SCANPY: Large-scale single-cell gene expression data analysis. *Genome Biol.* **19**, 15 (2018).
69. H. Li, R. Durbin, Fast and accurate short read alignment with Burrows-Wheeler transform. *Bioinformatics* **25**, 1754–1760 (2009).
70. A. McKenna, M. Hanna, E. Banks, A. Sivachenko, K. Cibulskis, A. Kernytsky, K. Garimella, D. Altshuler, S. Gabriel, M. Daly, M. A. DePristo, The Genome Analysis Toolkit: A MapReduce framework for analyzing next-generation DNA sequencing data. *Genome Res.* **20**, 1297–1303 (2010).
71. H. Li, B. Handsaker, A. Wysoker, T. Fennell, J. Ruan, N. Homer, G. Marth, G. Abecasis, R. Durbin; 1000 Genome Project Data Processing Subgroup, The Sequence Alignment/Map format and SAMtools. *Bioinformatics* **25**, 2078–2079 (2009).
72. K. Wang, M. Li, H. Hakonarson, ANNOVAR: Functional annotation of genetic variants from high-throughput sequencing data. *Nucleic Acids Res.* **38**, e164 (2010).
73. M. I. Love, W. Huber, S. Anders, Moderated estimation of fold change and dispersion for RNA-seq data with DESeq2. *Genome Biol.* **15**, 550 (2014).
74. Y. Benjamini, Y. Hochberg, Controlling the false discovery rate: A practical and powerful approach to multiple testing. *J. R. Stat. Soc. B Methodol.* **57**, 289–300 (1995).
75. E. Afgan, D. Baker, B. Batut, M. van den Beek, D. Bouvier, M. Čech, J. Chilton, D. Clements, N. Coraor, B. A. Grüning, A. Guerler, J. Hillman-Jackson, S. Hiltemann, V. Jalili, H. Rasche, N. Soranzo, J. Goecks, J. Taylor, A. Nekrutenko, D. Blankenberg, The Galaxy platform for accessible, reproducible and collaborative biomedical analyses: 2018 update. *Nucleic Acids Res.* **46**, W537–W544 (2018).
76. E. Afgan, D. Baker, M. van den Beek, D. Blankenberg, D. Bouvier, M. Čech, J. Chilton, D. Clements, N. Coraor, C. Eberhard, B. Grüning, A. Guerler, J. Hillman-Jackson, G. von Kuster, E. Rasche, N. Soranzo, N. Turaga, J. Taylor, A. Nekrutenko, J. Goecks, The Galaxy platform for accessible, reproducible and collaborative biomedical analyses: 2016 update. *Nucleic Acids Res.* **44**, W3–W10 (2016).
77. D. Blankenberg, A. Gordon, G. von Kuster, N. Coraor, J. Taylor, A. Nekrutenko; the Galaxy Team, Manipulation of FASTQ data with Galaxy. *Bioinformatics* **26**, 1783–1785 (2010).
78. A. M. Bolger, M. Lohse, B. Usadel, Trimmomatic: A flexible trimmer for Illumina sequence data. *Bioinformatics* **30**, 2114–2120 (2014).
79. D. Kim, G. Pertea, C. Trapnell, H. Pimentel, R. Kelley, S. L. Salzberg, TopHat2: Accurate alignment of transcriptomes in the presence of insertions, deletions and gene fusions. *Genome Biol.* **14**, R36 (2013).
80. S. Anders, P. T. Pyl, W. Huber, HTSeq—A Python framework to work with high-throughput sequencing data. *Bioinformatics* **31**, 166–169 (2015).
81. M. Ashburner, C. A. Ball, J. A. Blake, D. Botstein, H. Butler, J. M. Cherry, A. P. Davis, K. Dolinski, S. S. Dwight, J. T. Eppig, M. A. Harris, D. P. Hill, L. Issel-Tarver, A. Kasarskis, S. Lewis, J. C. Matese, J. E. Richardson, M. Ringwald, G. M. Rubin, G. Sherlock, Gene ontology: Tool for the unification of biology. The Gene Ontology Consortium. *Nat. Genet.* **25**, 25–29 (2000).
82. Gene Ontology Consortium, The Gene Ontology resource: Enriching a GOld mine. *Nucleic Acids Res.* **49**, D325–D334 (2021).
83. B. Langmead, S. L. Salzberg, Fast gapped-read alignment with Bowtie 2. *Nat. Methods* **9**, 357–359 (2012).
84. J. Feng, T. Liu, B. Qin, Y. Zhang, X. S. Liu, Identifying ChIP-seq enrichment using MACS. *Nat. Protoc.* **7**, 1728–1740 (2012).
85. G. Yu, L. G. Wang, Q. Y. He, ChIPseeker: An R/Bioconductor package for ChIP peak annotation, comparison and visualization. *Bioinformatics* **31**, 2382–2383 (2015).
86. S. Neph, M. S. Kuehn, A. P. Reynolds, E. Haugen, R. E. Thurman, A. K. Johnson, E. Rynes, M. T. Maurano, J. Vierstra, S. Thomas, R. Sandstrom, R. Humbert, J. A. Stamatoyannopoulos, BEDOPS: High-performance genomic feature operations. *Bioinformatics* **28**, 1919–1920 (2012).
87. A. Lex, N. Gehlenborg, H. Strobelt, R. Vuillemot, H. Pfister, UpSet: Visualization of intersecting sets. *IEEE Trans. Vis. Comput. Graph.* **20**, 1983–1992 (2014).
88. J. T. Robinson, H. Thorvaldsdóttir, W. Winckler, M. Guttman, E. S. Lander, G. Getz, J. P. Mesirov, Integrative genomics viewer. *Nat. Biotechnol.* **29**, 24–26 (2011).
89. J. P. Lambert, M. Tucholska, C. Go, J. D. Knight, A. C. Gingras, Proximity biotinylation and affinity purification are complementary approaches for the interactome mapping of chromatin-associated protein complexes. *J. Proteomics* **118**, 81–94 (2015).
90. R. Hand, D. Bortone, P. Mattar, L. Nguyen, J. I.-T. Heng, S. Guerrier, E. Boutt, E. Peters, A. P. Barnes, C. Parras, C. Schuurmans, F. Guillemot, F. Polleux, Phosphorylation of Neurogenin2 specifies the migration properties and the dendritic morphology of pyramidal neurons in the neocortex. *Neuron* **48**, 45–62 (2005).
91. S. Irie, R. Sanuki, Y. Muranishi, K. Kato, T. Chaya, T. Furukawa, Rax homeoprotein regulates photoreceptor cell maturation and survival in association with Crx in the postnatal mouse retina. *Mol. Cell. Biol.* **35**, 2583–2596 (2015).
92. K. J. Roux, D. I. Kim, M. Raida, B. Burke, A promiscuous biotin ligase fusion protein identifies proximal and interacting proteins in mammalian cells. *J. Cell Biol.* **196**, 801–810 (2012).

Acknowledgments: We thank all the patients and their families for their enthusiastic participation. We are grateful to J. Drouin, K. Khetchoumian, and A. Balsalobre for help with the POMC-luciferase assays. We thank Z. Cayouette for the artistic rendering of the retinal degeneration index analysis shown in Fig. 7E and B. Boulan for help with automated cell counting in ImageJ. We thank J. Cross, T. Furukawa, A.-C. Gingras, S. Henikoff, D. Hodzik, C. Schuurmans, G. Thiel, L. Tiberi, and P. Vanderhaeghen for sharing plasmids. We also thank C. Davis, L. Haer-Wigman, A. Tracewska-Siemiatkowska, and F. Cremers for their support; I. Lopez for her coordinating efforts; L. S. Sullivan for invaluable technical assistance; J. Barthe for mouse colony management; D. Faubert for help with mass spectrometry; C. Poitras for help with BioID analysis; and O. Neyret for help with RNA-seq and CUT&RUN experiments. **Funding:** This work was funded by grants from the NIH (R01HD084459 to V.J.B. and R01-030499-01 to R.K.K.), the Canadian Institutes of Health Research (to R.K.K. and M.C.; FDN-159936), Fighting Blindness Canada (to R.K.K. and M.C.), FRQS Vision Health Research Network (to R.K.K.), and the Montreal Children's Hospital Foundation (to R.K.K.). Additional funding: The National Science Foundation of China grant (81873687) and CAMS innovation fund for medical sciences (CIFMS 2016-12 M-1-002) to R.S. This work was also supported by grants from the National Eye Institute (R01EY022356 and R01EY018571 to R.C.), the NIH (EY007142), the Foundation Fighting Blindness, and the William Stamps Farish Fund (to S.P.D.). L.T. received funding from The Research Foundation at Mo Gård. M.C. is an Emeritus Scholar from the FRQS and holds the Gaëtane and Roland Pillenière Chair in Retina Biology from the IRCM Foundation. **Author contributions:** Conceptualization: M.L., C.Jo., R.K.K., and M.C. Data curation: M.L., C.Jo., A.J., P.M., M.D.G., S.P.D., M.B., L.T., N.D.R., K.G., C.Je., R.C., Z.S., H.L., N.A., and J.M. Formal analysis: M.L., C.Jo., P.M., and A.J. Investigation: M.L., C.Jo., P.M., A.J., Z.S., and H.L. Project administration: M.L., C.Jo., R.S., R.K.K., and M.C. Resources: M.L., C.Jo., M.D.G., P.M., A.J., V.J.B., R.S., R.K.K., and M.C. Funding acquisition: V.J.B., R.S., R.K.K., and M.C. Supervision: V.J.B., R.K.K., and M.C. Visualization: M.L., C.Jo., R.K.K., and M.C. Writing—original draft: M.L., C.Jo., and M.C. Writing—review and editing: All authors. **Competing interests:** The authors declare that they have no competing interests. **Data and materials availability:** All data needed to evaluate the conclusions in the paper are present in the paper and/or the Supplementary Materials. RNA-seq and CUT&RUN genomic data are available through Gene Expression Omnibus (GEO) with accession numbers GSE156756 for CUT&RUN IgG control and GSE168129 for BCOR, and Otx2 CUT&RUN, as well as shBcor and control RNA-seq. Proteomics data (IP-MS and BioID) will be submitted to MassIVE.

Submitted 1 March 2021
Accepted 21 July 2022
Published 7 September 2022
10.1126/sciadv.abh2868